Ephemeral grounding on the Pine Island Ice Shelf, West Antarctica, from 2014 to 2023

~~Yide Qian[1]~~Yite Chien[1,2,3], Chunxia Zhou[1,2,3*], Sainan Sun[4], Yiming Chen[1,2,3], Tao Wang[1,2,3], Baojun Zhang[1,2,3]

[1]Chinese Antarctic Center of Surveying and Mapping, Wuhan University, Wuhan, 430079, China
[2]Key Laboratory of Polar Environment Monitoring and Public Governance (Wuhan University), Ministry of Education, Wuhan, 430079 China
[3]School of Geodesy and Geomatics, Wuhan University, Wuhan, 430079 China
[4]Department of Geography and Environmental Sciences, Northumbria University, Newcastle upon Tyne, NE1 8ST, UK

Correspondence to: Chunxia Zhou (zhoucx@whu.edu.cn)

Abstract. ~~Ephemeral grounding~~ The evolution of ephemeral grounding in ice shelf can affect buttressing, alter ice flow dynamics, and influence ice shelf stability. Long-term observations of ephemeral grounding sites ~~form when ice shelves thin or relative sea level rises, causing pinning points to ground intermittently over~~ are crucial for understanding how thickness, basal conditions, and tidal ~~cycles.~~interactions evolve over time. Vertical ~~displacements~~displacement data derived from Sentinel-1A/B imagery ~~reveal~~reveals the ~~ephemeral grounding 10~~ history of ~~the Pine Island Ice Shelf~~ephemeral grounding events at PIIS from 2014 to 2023. ~~We found that~~ Our results suggest that ephemeral grounding at an ice rumple is modulated by the interaction between tidal forcing, ice shelf thickness, and evolving sub-ice-shelf geometry. A prominent central keel, shaped by inherited bed topography, promotes repeated contact with a submarine ridge. Landsat-8 images reveal that the ~~ephemeral grounding site disappeared after~~rifts that cause the ~~ice shelf calved in~~ 2020 ~~and appeared again after October 2021. We conclude that basal melting directly influences~~ calving event may have formed due to the ~~occurrence of ephemeral~~ice shelf grounding at the ~~central ice shelf. Ice shelf calving and atmospheric forcings, such as La Niña and~~ study site. These findings provide new insights into the ~~positive phase of the Antarctic Oscillation, are indirect factors that affect ephemeral grounding. We propose that the~~mechanisms driving ephemeral grounding ~~site at the central ice shelf may evolve into a final pinning point~~behaviour and ~~may influence future ice shelf calving events. 15 Further studies on~~highlight its potential role in modulating ice shelf ~~modeling are needed to understand the interaction between ephemeral grounding and rift propagation.~~stability.

1 Introduction

Ice discharge from the Antarctic Ice Sheet is a major contributor to global sea-level rise. (Shepherd et al., 2012; Bamber et al., 2018; Smith et al., 2020). Ice This discharge is regulated in part by ice shelves act as crucial buttresses, resisting the , which exert a buttressing that resists upstream ice flow of inland ice into the ocean. However, in many regions, the buttressing capacity of ice shelves has been reduced by processes such as ice shelf thinning and , calving events, grounding line retreat, unpinning from topographic highs, and the disintegration of shear margins (Fürst et al. 2016; Gudmundsson et al., have significantly reduced their buttressing capacity, leading2019; Lhermitte et al., 2020; Miles and Bingham, 2024; Walker et al., 2024; Fricker et al., 2025).

A prominent example of these dynamics can be seen in the Amundsen Sea sector of West Antarctica, which accounts for over 31% of the continent's total ice loss. Within this sector, the Pine Island Glacier (PIG) basin alone contributed approximately 3.0 mm to accelerated ice discharge and an increased contribution to global sea-level rise (Rottbetween 1979 and 2017 (Smith et al., 2002, 20182020; Rignot et al., 2019). The PIG ice front has retreated approximately 26 km since 2015, with calving frequency increasing from intervals of about six years to every one to two years (Depoorter et al., 2013; Mouginot et al., 2014; Paolo et al., 2015; Arndt et al., 2018; Shepherd et al., 2018; Qi et al., 2004; Pritchard et al., 2012; Fürst et al.,2021; 2016; Gudmundsson et al., 2019; Joughin et al., 2021). Following three major calving events in 2017, 2018, and 2020, the ice shelf experienced a >12% speedup relative to 2017, coinciding with a 19 km retreat of the ice front (Joughin et al., 2021).

The recent dynamic changes at PIG have been driven mostly by enhanced basal melting, caused by the intrusion of warm Circumpolar Deep Water (CDW) beneath the ice shelf (Jenkins et al., 2010; Jacobs et al., 2011; Pritchard et al., 2012; Hillenbrand et al., 2017; Smith et al., 2017; Davies et al., 2017; Shean et al., 2019). 2021). This buttressing effect is primarily controlled by resistive forces, including lateral drag This oceanic forcing initially caused transient grounding of the central ice shelf on a submarine ridge from the 1940s through the 1970s, followed by complete ungrounding between 1973 and 1989 (Jenkins et al., 2010; Smith et al., 2017; Miles and Bingham, 2024). Continued ice shelf thinning subsequently drove an ~8.7 km retreat of the grounding line along the main trunk between 1992 and 2009, resulting in further ungrounding from an ice plain (Corr et al., 2001; Joughin et al., 2010; Dutrieux et al., 2014a; Rignot et al., 2014). Despite the grounding line retreat, the Pine Island Ice Shelf (PIIS) was observed to maintain intermittent contact with the bathymetric high when thick ice column being advected from the upstream deep trough (Joughin et al., 2016; Lowery et al., 2025). This region is referred to as ice rumple L (Figure 1) in the study by Rignot et al. (2014). This ephemeral grounding is now attributed to interactions between sub-ice keels and a submarine ridge (Graham et al., 2013; Joughin et al., 2016; Shean, 2016; Davies et al., 2017embayment walls and the resistance offered by pinning points, where ice shelves ground on elevated seafloor features (Matsuoka et al., 2015; Alley et al., 2015).

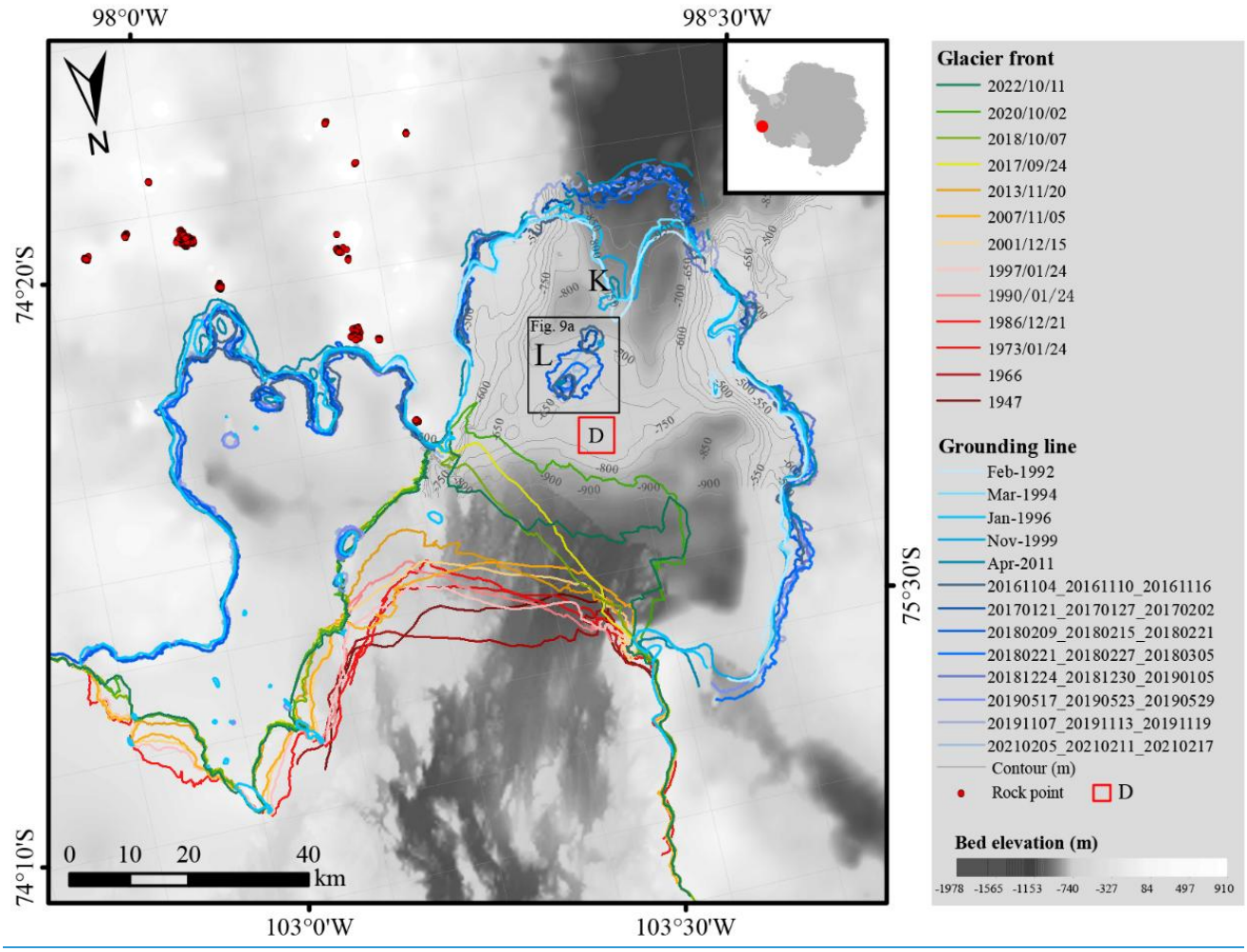

Figure 1. Location and geometry of the PIIS. ~~Pinning~~Ice front positions, grounding line locations, and 458 non-glaciated ground control points (red points). Bed elevation (50 m contour interval, labelled between -750 m and -500 m) is from BedMachine v3 (Morlighem et al., 2020; Morlighem, 2022), showing the submarine ridge. Grounding lines are from MEaSUREs (Rignot et al., 2016) (from 1992 to 2011) and from DROT results (from 2016 to 2021). L and K mark ice rumples (Rignot et al., 2014). Ice front positions for 1947 and 1966 are from Rignot (2002); later positions (1973-2022) are from Landsat ~~are critical~~ imagery (Landsat-1/4/5/7/8/9) and Sentinel-1 SAR imagery via Google Earth Engine. Red block D denote the region for calculating mean double-differential vertical displacement. The black frame denotes the zoomed-in ~~modulating~~region in Figure 9a.

Ephemeral grounding could be driven by tidal cycles, ice shelf ~~dynamics (Matsuoka et al., 2015). Their evolution, particularly changes in size and location, can significantly influence ice flow by inducing lateral and basal shear stresses, as well as upstream compression and downstream tension (Fried et al., 2014; Still et al., 2019, 2021). Additionally, pinning points can promote rifting and calving, further reducing buttressing (Arndt et al., 2018), and can alter sub-ice shelf ocean circulation and basal melt patterns (Milillo et al., 2019; Shean et al., 2019). Over time, some pinning points have disappeared entirely, particularly since 1973 (Milles and Bingham, 2024). As ice shelves thin~~thinning or ~~relative~~thickening, sea ~~levels~~-level rise,

these features may transition into ephemeral grounding sites, where grounding occurs only intermittently during tidal cyclesand sea-level fall—depending on prior grounding conditions (Schmeltz et al., 2001; Rignot, 2002; Matsuoka et al., 2015). Although the direct The grounding of ice shelf on high bathymetry features could impact ice dynamics as an obstacle against ice flow: 1) enhance the buttressing effect of ephemeral grounding sites is minimal, their presence and evolution provide valuable insights into changes in by providing back stress against upstream ice; 2) facilitate fracturing and ice shelf thickness and basal drag, which can influence surface elevation and larger-scale ice shelf dynamics weakening in response to stress associated with grounding (Rignot, 2002; Christianson et al., 2016; Jeong et al., 2016; Shean, 2016; Benn et al., 2022; Wang et al., 2025).

A prominent example of ephemeral grounding is ice rumple L, a 0.5-km-diameter feature on the central Pine Island Ice Shelf (PIIS) (Figure 1). First observed in 2011 using differential interferometry (Rignot et al., 2014), ice rumple L is believed to have become ephemerally grounded in the 1940s and fully ungrounded between 1973 and 1989 (Jenkins et al., 2010; Smith et al., 2017; Milles and Bingham, 2024). This ungrounding has been attributed to increased basal melting caused by the intrusion of warm Circumpolar Deep Water (CDW) (Jenkins et al., 2010; Jacobs et al., Satellite remote sensing can effectively detect transient vertical 2011; Pritchard et al., 2012; Hillenbrand et al., 2017; Smith et al., 2017; Davies et al., 2017; Shean et al., 2019). Ice rumple L reappeared after 2011, and its recurring cycle of ephemeral grounding is now understood to result from interactions between sub-ice shelf keels and an underlying submarine ridge (Graham et al., 2013; Joughin et al., 2016; Shean, 2016; Davies et al., 2017). After four calving events occurred between 2015 and 2020 (Jeong et al., 2016; Arndt et al., 2018; Qi et al., 2021), specifically on July 13, 2015, October 12, 2017, October 31, 2018, and February 11, 2020, the changes to ice rumple L remain unclear.

Vertical motion of ice shelves, particularlyespecially tidal fluctuations associated withthat cause ephemeral grounding, can be observed using several satellite techniques, including. Key methods include differential range offset tracking (DROT) (Marsh et al., 2013; Joughin et al., 2016; Christianson et al., 2016; Wallis et al., 20242024, 2025; Lowery et al., 2025; Zhu et al., 2025), interferometric synthetic aperture radar (InSAR) (Schmeltz et al., 2001; Rignot, 2002, 2014), and satellite altimetry (Fricker and Padman, 2006). However, the rapid motion of ice shelves presents a challenge for traditional Both DROT and InSAR, requiring methods in theory indicate the landward limit of tidal flexure. While InSAR is widely used to map grounding line migration, its effectiveness is limited in fast-flowing areas due to phase aliasing unless very short repeat cycles to avoid phase aliasing (Rignot et al., 2014; Scheuchl et al., 2016; Milillo et al., 2017).intervals are available. For instance, Milillo et al. (2017) used 1-day repeat COSMO-SkyMed data to studytrack grounding line changes at PIIS.

In contrast, DROT offers an alternative, as itprovides a complementary approach that does not rely on phase information. This makes it particularly well-suited, making it useful for observing vertical tidal displacements on fast-moving ice shelves, even though it may bedespite being less precise than InSAR in some contexts (Marsh et al., 2013; Hogg, 2015; Joughin et al., 2016; Christianson et al., 2016; Friedl et al., 2020; Wallis et al., 2024).; Lowery et al., 2025; Zhu et al., 2025). Using TerraSAR-X

data, Joughin et al. (2016), using DROT with TerraSAR-X SM data (11- or 22-day repeat, ~3 m range resolution),(2016) identified a vertical displacement anomaly near ice rumple L, achieving a grounding line position precision of approximately 1.5 km. More recently, from November 2013 to November 2015. At Petermann Glacier, Friedl et al. (2020) and Wallis et al. (2024) have demonstrated the effectiveness of DROT with Sentinel-1 IW data for grounding line studies. According to Friedl et al. (2020),found DROT-derived grounding line positions (tidal flexure limit) werelimits ~2 km seaward of DInSAR results. More recently, DROT applied to Sentinel-1 IW data has proven effective for studying grounding line and pinning point dynamics on the Antarctic Peninsula (Wallis et al., 2024), Amery Ice Shelf (Zhu et al., 2025), and ~2 km landward of H positions, where isPIIS (Lowery et al., 2025). However, Lowery et al. (2025) focused only on the landward limit of stable hydrostatic equilibriumyear 2017, leaving later changes unresolved. Thus, the evolution of grounding behaviour at ice rumple L following four subsequent calving events—in 2015, 2017, 2018, and 2020—remains poorly understood.

To address the knowledge gap regarding the relationship between changes of ice rumple L and ice shelf dynamics at PIIS, particularly in the period following four recent calving events and an observed increase in ice velocity from 2014 to 2023analyze double-differential vertical displacement derived from Sentinel-1 SAR data, which provides consistent spatial and temporal coverage of the region. Combined with time series of ice thickness change from 2010 to 2021 derived from REMA DEM (Howat et al., 2022a), we aim to reconstruct the ephemeral grounding history of the PIIS from 2014 to 2023 and investigate the influence of calving, oceanic forcing and atmospheric forcings on ephemeral grounding.

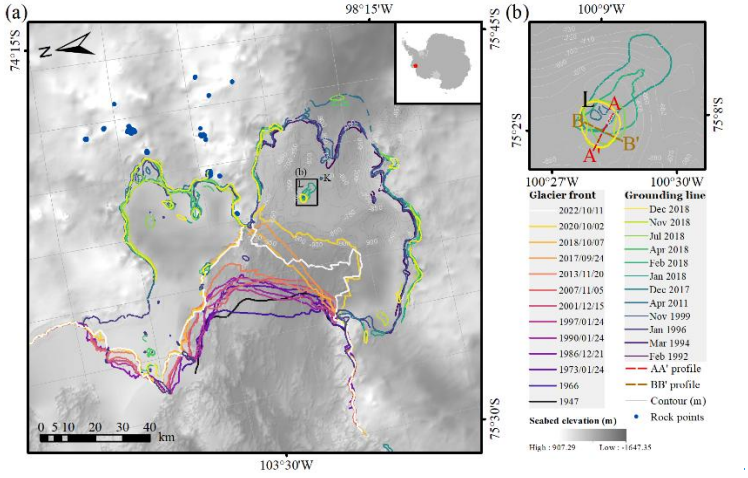

Figure 1. Location and geometry of the PIIS. (a) Ice front positions, grounding line locations, and 458 non-glaciated ground control points 65 (blue) on the PIIS. (b) Ice rumple L, the 2011 grounding line, and profiles AA' and BB' used for ice-equivalent freeboard thickness change analysis. Bathymetry (50 m contour interval, labeled between -750 m and -500 m) is from BedMachine v3 (Morlighem et al., 2020; Morlighem, 2022), showing the submarine ridge. Grounding lines are from MEaSUREs (Rignot et al., 2016), ESA CCI (Floricioiu et al., 2021), and Mohajerani et al. (2021). L and K mark ice rumples (Rignot et al., 2014). Ice front positions for 1947 and 1966 are from Rignot (2002); later positions (1973–2022) are from Landsat panchromatic imagery and Sentinel-1 SAR imagery via Google Earth Engine.

To address this gap, we reconstruct the grounding history of PIIS from 2014 to 2023 using DROT applied to Sentinel-1A/B SAR data. We combine these observations with a 2010–2021 time series of ice thickness change derived from Reference Elevation Model of Antarctica (REMA) DEM (Howat et al., 2022a) and ICESat-2 ATL06 data (Smith et al., 2019; Smith et al., 2023) to examine the link between ephemeral grounding at ice rumple L and recent changes in ice shelf dynamics. This dataset provides spatially and temporally consistent coverage across the PIIS.

2 Methods and Data

2.1 Double-differential vertical displacement calculation

Vertical displacement maps were generated for the ~~Pine Island Glacier (~~PIG~~)~~ basin using the intensity offset tracking algorithm ~~in GAMMA software.~~ This involved applying the algorithm to ~~426~~420 scenes of Sentinel-1A/B ascending imagery, covering periods of 6- or 12-days from October 2014 to December 2023. Details of the imagery used are provided in Table 1. Processing steps are outlined in Figure 2. We applied fine ~~coregistration~~co-registration and ~~deramping~~de-ramping procedures prior to offset tracking (Wegmüller et al., 2016; Sánchez-Gámez et al., 2017; Chen et al., 2020). We used the REMA ~~dataset~~200 m mosaic DEM (Howat et al., 2019; 2022b), which is posted on a 200 m grid, as the reference DEM for geocoding and ~~coregistering~~co-registering the Sentinel-1 imagery. To compute the displacement fields from the ~~coregistered~~co-registered and ~~deramped~~de-ramped imagery, we propose a 2D cross-correlation window of 480×96 (range × azimuth) pixels with step sizes of 100 and 20 pixels in the azimuth and range directions, respectively. We used the REMA 200 m mosaic DEM to geocode the displacement maps based on bicubic-log spline interpolation. The final vertical displacement maps and velocity maps were generated on 100 m×100 m grids and geocoded to the Antarctic Polar Stereographic Projection (EPSG:3031).

Table 1. Sentinel-1A/B images used in this study

Path/frame	Date	~~Image~~Numbers of image pairs
65/909	2014/10/10 – 2015/11/10 2016/05/20 – 2017/06/20	76
65/908	2015/11/22 – 2016/07/07	17
65/910 and 65/911	2017/06/14 – 2024/01/03	327
	Total	420

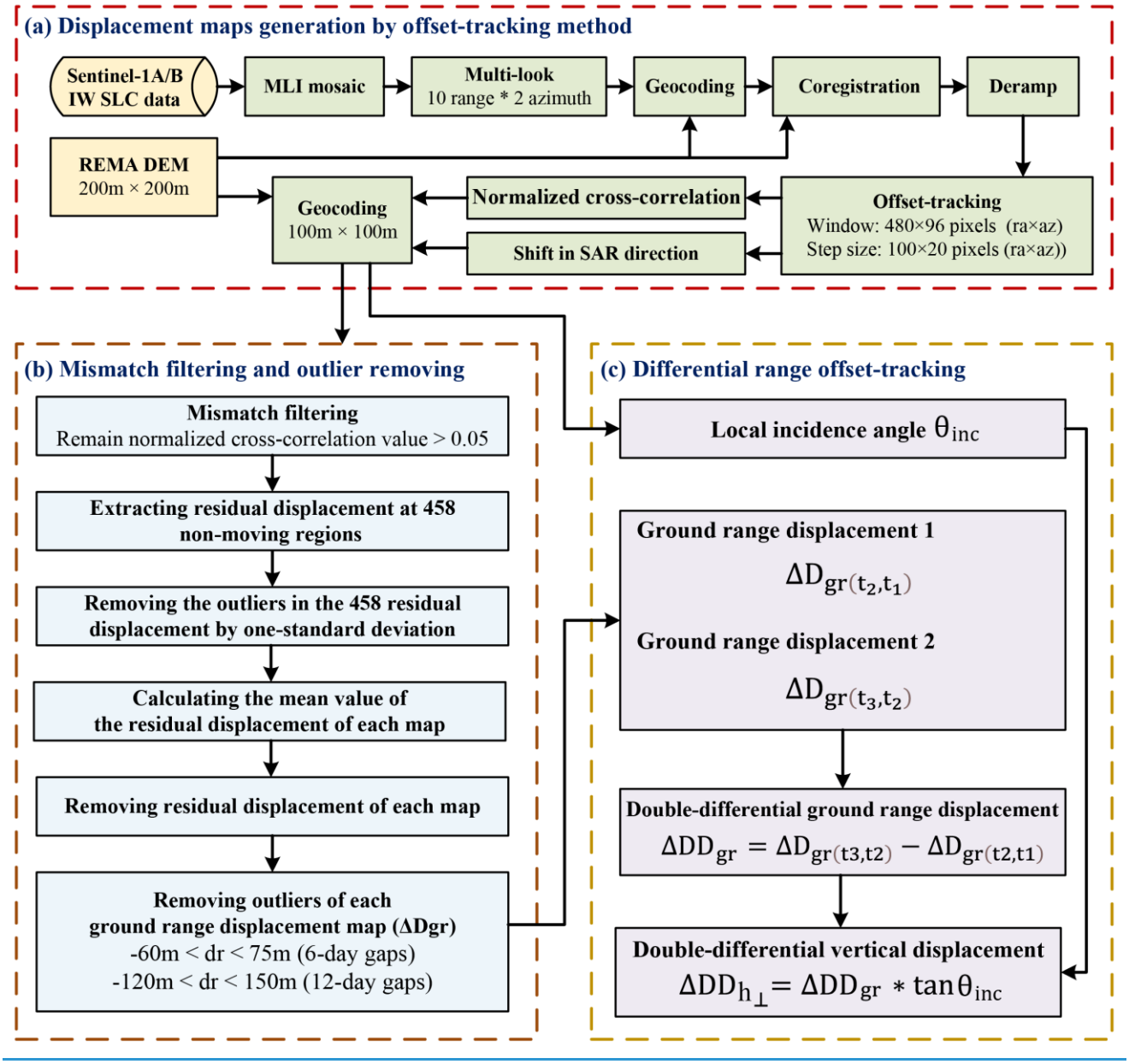

Figure 2. Processing steps of range displacement generation and DROT.

To reduce noise and remove outliers ~~(Paul et al., 2015; Lemos et al., 2018; Solgaard et al., 2021; Lei et al., 2021),~~in the Sentinel-1 offset tracking data, we ~~first accepted~~employed a multi-step filtering and calibration approach. First, we retained only pixels with ~~an NCC~~ a normalized cross-correlation value greater than 0.05~~.~~, which also used by Solgaard et al. (2021) to ensure reliable displacement measurements. Second, we extracted the residual displacement at 458 widely distributed, non-moving points over the exposed bedrock (Figure 1~~(a)), removed outliers~~). Outliers beyond one standard deviation~~, and~~

~~calculated the mean value~~ were removed, following the same criteria that used in Chen et al. (2020), and the mean residual displacement for each time interval~~. Third, we calibrated the ice displacement by subtracting the mean value of~~ was calculated and used to calibrate the ~~residual displacement. Finally~~displacement maps by subtracting this mean value. To further remove noise and erroneous measurements, we examined the distribution of azimuth and range displacements across the entire time series ~~and identified the highest and lowest displacement values.~~(Figure S1) and established empirical thresholds based on reasonable minimum and maximum velocities of ice movement at PIIS. We ~~then~~ invalidated pixels with ~~the following criteria: azimuth displacement values less than -30 m or greater than 90 m for a 6-day gap; azimuth displacement values less than -60 m or greater than 180 m for a 12-day gap; range displacement values~~slant range displacements less than -60 m or greater than 75 m for ~~a~~ 6-day ~~gap;~~gaps, and ~~range displacement values~~ less than -120 m or greater than 150 m for ~~a 12-day gap~~12-day gaps, which can exclude a small portion of pixels and improved the consistency and quality of the final displacement fields.

The slant range displacement fields generated over floating ice contain both horizontal displacement and bias due to vertical ocean motion. When the SAR sensor observes an object $P_{(x,y)}$ from the same location in orbit, the SAR sensor can detect vertical displacement in the slant range direction ($\Delta D_{sr(t_2,t_1)}$ in Figure ~~2~~3):

~~$$\Delta D_{sr(t_2,t_1)} = D_{sr(t_2)} - D_{sr(t_1)} \quad (1)$$~~

where D_{sr} is the distance between the object $P_{(x,y)}$ and the SAR sensor; t_1 and t_2 reflect the acquisition time of the master image and the acquisition time of the slave image, respectively. The magnitude of the observed slant range displacement depends on the local incidence angle (~~θ_{inc}~~),θ_{inc}), which is defined as the angle between the incident radar signal and the local surface normal, expressed in radians When the slant range displacement is converted to ground range displacement, the additional displacement in the ground range ($\Delta D_{gr(t_2,t_1)}$) equals the vertical change (~~$\Delta h_{\perp(t_2,t_1)}$~~$\Delta h_{\perp(t_2,t_1)}$) divided by ~~$\tan\theta_{inc}$~~ $\tan\theta_{inc}$:

~~$$\Delta D_{gr(t_2,t_1)} = \frac{\Delta h_{\perp(t_2,t_1)}}{\tan\theta_{inc}} \quad (2)$$~~

$$\Delta D_{gr(t_2,t_1)} = \frac{\Delta h_{\perp(t_2,t_1)}}{\tan\theta_{inc}} \quad (2)$$

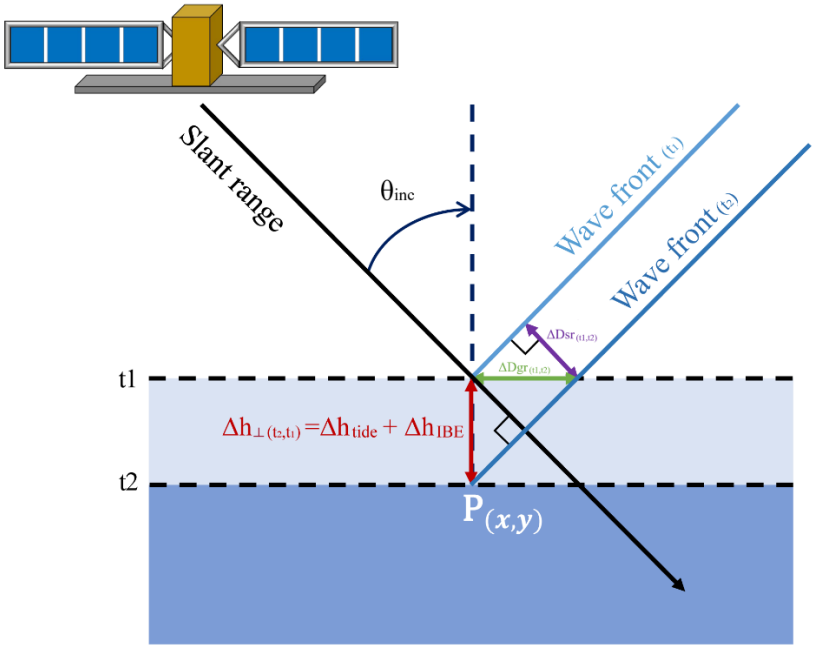

Figure ~~2~~3. Side-looking spaceborne SAR imaging geometry. A vertical displacement of a Point $P_{(x,y)}$ from t_1 to t_2 is imaged at different slant range positions (~~$\Delta D_{sr(t_2,t_1)}$~~$\Delta D_{sr(t_2,t_1)}$) depending on its elevation.

Assuming ~~that~~ the horizontal displacement between two SAR image pairs that are closely spaced in time is very small, we can cancel the horizontal displacement and obtain the differential vertical bias in the ground range (~~ΔDD_{gr}~~ΔDD_{gr}) by differencing two ground range displacement fields (Rignot, 1998; Joughin et al., 2010; Marsh et al., 2013; Christianson et al., 2016; Joughin et al., 2016; Friedl et al., 2020):

~~$$\Delta DD_{gr} = \Delta D_{gr(t3,t2)} - \Delta D_{gr(t2,t1)} \quad (3)$$~~

where ~~$\Delta D_{gr(t_2,t_1)}$~~$\Delta D_{gr(t_2,t_1)}$ and $\Delta D_{gr(t_3,t_2)}$ are the vertical displacement differences in the ground range direction from the displacement map generated from the acquisition dates t_1 and t_2, and the acquisition dates t_2 and t_3, respectively. Therefore, the double differential vertical displacement (~~$\Delta DDh_{\perp}$~~$\Delta DD_{h_\perp}$) can be calculated as the double differential vertical bias in the ground range (~~ΔDD_{gr}~~ΔDD_{gr}) from both image pairs multiplied by ~~$\tan\theta_{inc}$~~$\tan\theta_{inc}$:

~~$$\Delta DDh_{\perp} = \Delta DD_{gr} * \tan\theta_{inc} \quad (4)$$~~

The REMA DEM was used consistently for both θ_{inc} (in radians) estimation and as the external DEM for co-registration in the offset tracking process, ensuring uniform referencing across displacement fields. The θ_{inc} was calculated for the first acquisition of each image pair. The local surface normal was derived from the REMA 200 m mosaic DEM. The vertical displacement caused by tidal forcing has minimal impact on the ice shelf's overall surface slope. While slope-induced errors are most significant in areas with localized topographic variability, ephemeral grounding events produce range-direction

displacement anomalies that exceed those caused by background slope variations, making these events clearly distinguishable. Consequently, we are confident that using a time-invariant DEM does not compromise the accuracy of our results, as the impact of slope variability on θ_{inc} and the resulting displacement estimates remains minimal.

Double-differential vertical displacement maps of PIIS were produced using differential range offset tracking, applied to slant range displacement fields. Ephemeral grounding events, indicated by near-zero displacement in the maps (Figure ~~3(a) (~~4a-c~~))~~) and flattened interferometric fringes in DInSAR (Figure ~~3(d)),~~4d), resulted in visible ~~'spots."~~'spots'. We ~~analyzed~~analysed each displacement map, noting dates with clear 'spots' at central PIIS, where the area around ~~Ice~~ice rumple L exhibited near-zero displacement (Figure ~~3(a)~~4a and ~~3(c)). Ephemeral grounding events were~~4c). Red block D in Figure 1 denote the region for extracting mean double-differential vertical displacement time series. The double-differential vertical displacement time series was compared with double-differential tidal height time series ~~(Figure 4(b)),~~ derived from the CATS2008_v2023 ocean tide model (~~Padman~~Howard et al., ~~2002~~2024) using Tide Model Driver 3.0 (Greene et al., 2023) at (-75.186576°S, -100.617021°W).

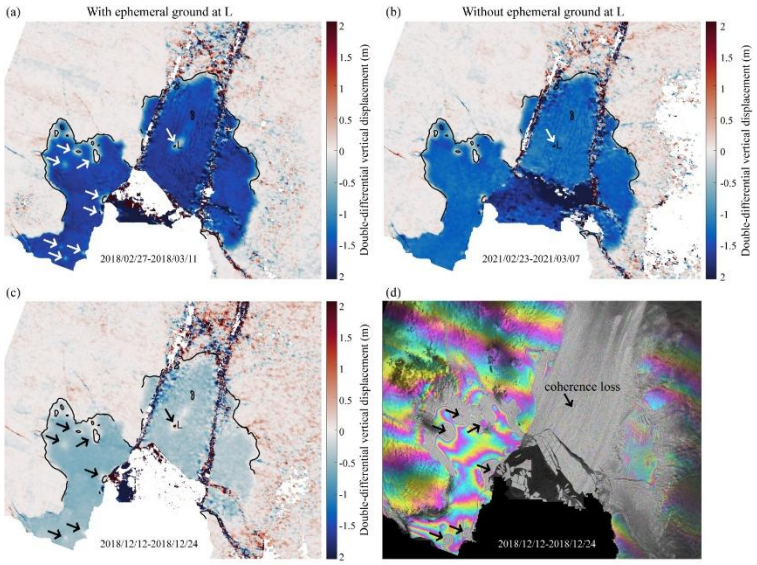

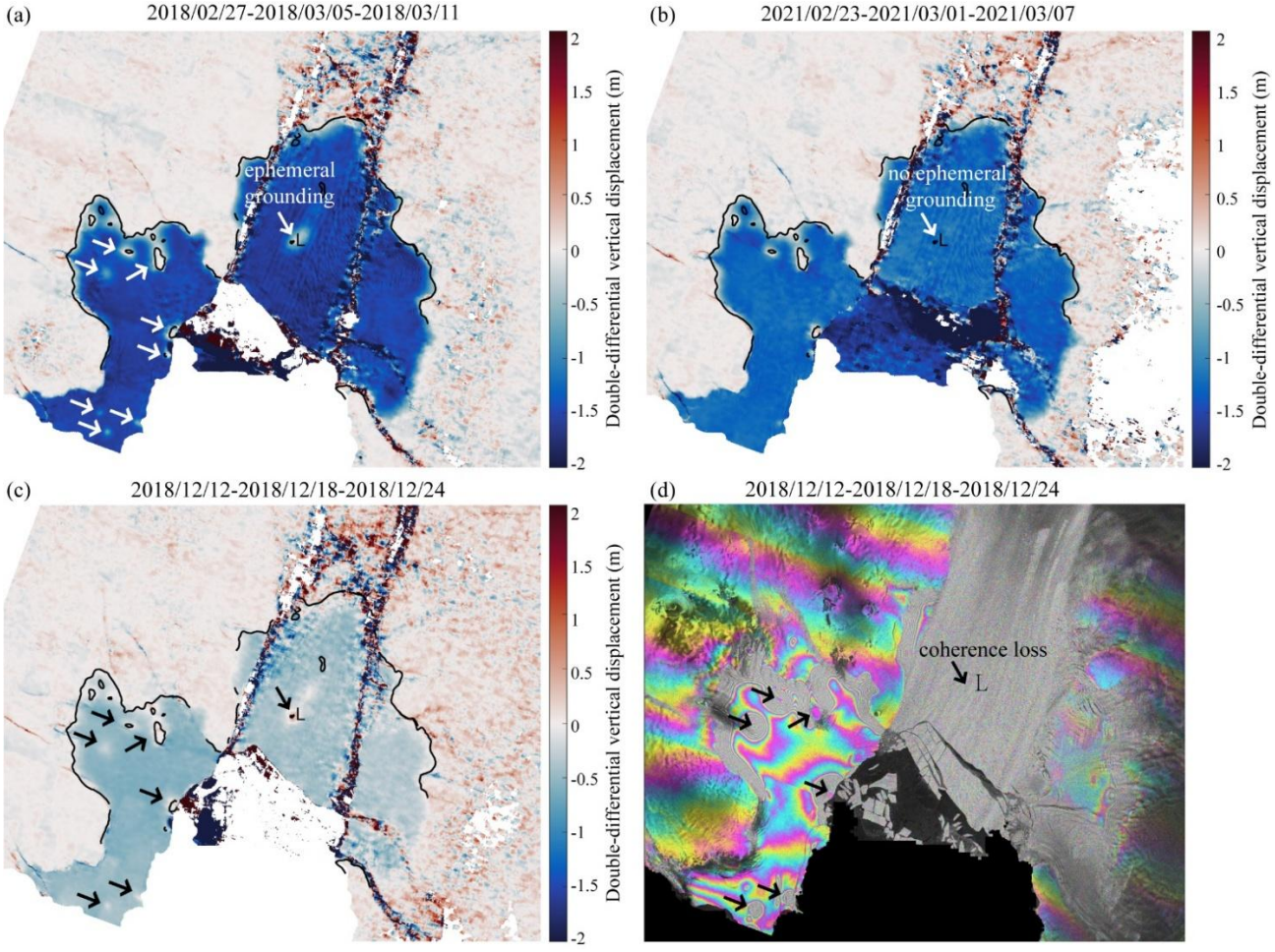

Figure 34. Double-differential vertical displacement compared with DInSAR interferogram, showing ephemeral grounding. (a) Double-differential displacement between 2018/02/27-2018/03/05 and 2018/03/05-2018/03/11. (b) Displacement between 2021/02/23-2021/03/01 and 2021/03/01-2021/03/07. (c) Displacement between 2018/12/12-2018/12/18 and 2018/12/18-2018/12/24. White arrows in (a) and (b), and black arrows in (c), indicate the location of ephemeral grounding, marked by near-zero displacement. (d) DInSAR interferogram for 2018/12/12-2018/12/18 and 2018/12/18-2018/12/24. ~~White and black~~Black arrows highlight ~~the~~ ephemeral grounding ~~location, marked by near-zero displacement~~sites at the northern PIIS. The DInSAR interferogram fails to capture this signal at ~~Ice~~ice rumple L due to coherence loss.

We extracted grounding line positions using Otsu's method (Otsu, 1979), which determines an optimal global threshold to convert each grayscale image into binary format. Following thresholding, morphological operations were applied to fill holes and close gaps. Grounding line positions were then extracted from the processed binary images.

2.2. REMA ~~DSM~~strips data correction

~~The REMA DSM 2-m strips from October 2010 to December 2022 were corrected by~~ Elevation data from the CryoSat-2 Baseline-D Level 2 ~~SARin~~SARIn product (Meloni et al., 2019), spanning from July 2010 to June 2022 ~~(Meloni et al., 2019)~~

and were coregistered through the code Basal melt rates Using REMA and Google Earth Engine (BURGEE) developed by Zinck et al. , were used to correct and co-register the REMA 2 m spatial resolution time-stamped DEM stripes(2023a, 2023b).

The REMA version 4.1 DSM 2 m strips are 13-year time series of elevation data derived from stereoscopic WorldView and GeoEye satellite imageryproduct, acquired frombetween October 2010 toand December 2022 (Howat et al., 2022). The DSM 2022b). These REMA strips are referenced to the WGS84 ellipsoid andbut are not coregistered with co-registered to satellite altimetry to increase their absolute accuracy. In accordance with Zinck et al. (2023a), the REMA 2 m DEM mosaic created from multiple strips that were coregistered with CryoSat-2 and ICESat (Howat et al., 2019) was used as the reference surface to exclude outliers. Using uncorrected REMA DSM data, we found surface elevation changes at PIIS exceeding 30 m (2010-2022); therefore, we tested elevation differences in the DEM mosaic, setting 100 m as the outlier filter criterion for REMA DSM strips and CryoSat-2 elevations.

We replaced the FES2004 ocean tide model provided by the ESA with the CATS2008 ocean tide model to provide a more accurate ocean loading tide by default. The correction and co-registration procedures were implemented using the "Basal melt rates Using REMA and Google Earth Engine (BURGEE)" processing framework developed by Zinck et al. (2023a, 2023b). value (Processing steps are outlined in Figure 5.

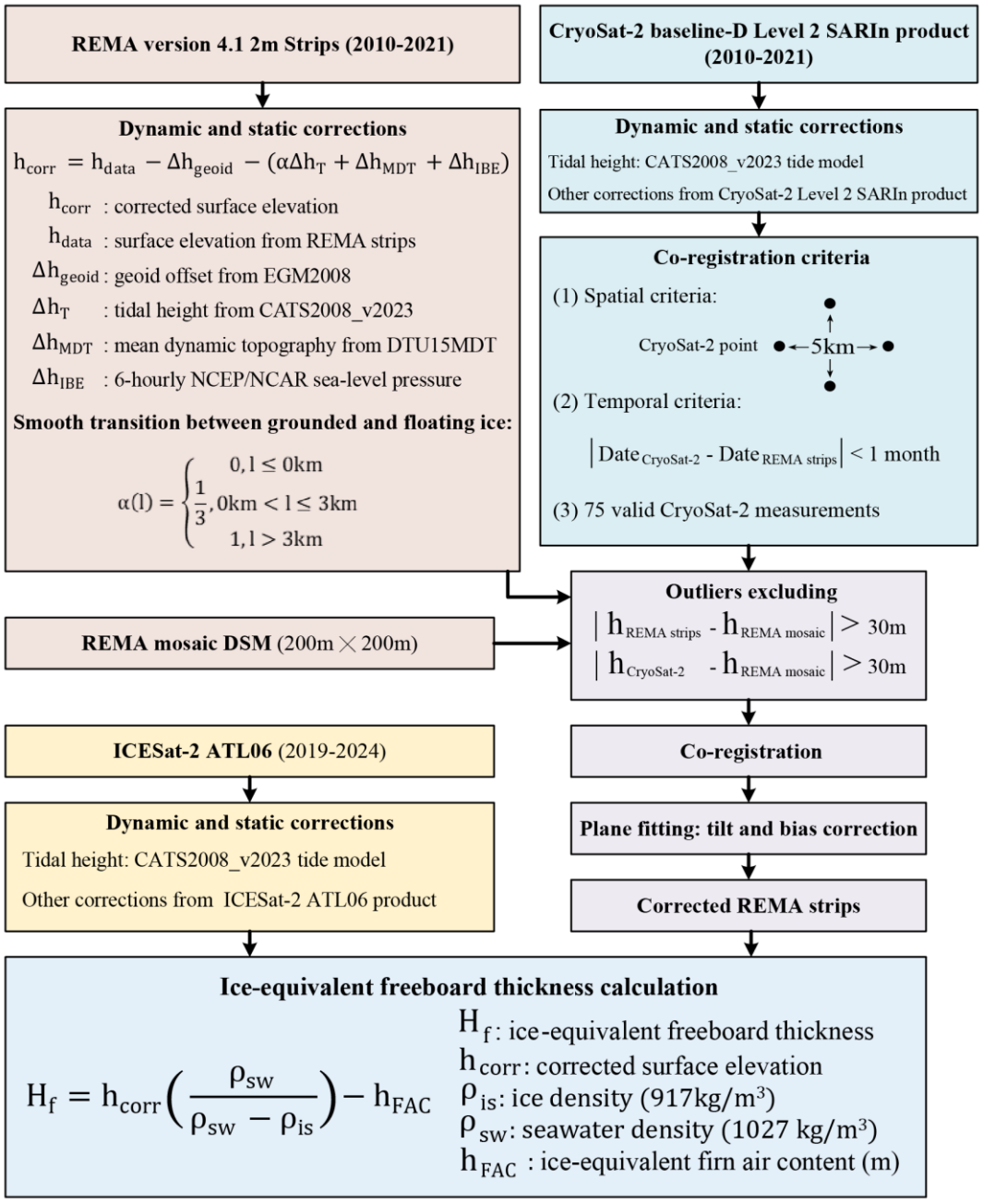

Figure 5. Processing steps for correction of REMA DEM, CryoSat-2, and ICESat-2 data.

Dynamic~~Zhang et al., 2020). For other corrections, such as solid earth tides, geocentric polar tides, and dry and wet tropospheric and ionospheric effects, we used the data provided by the ESA, as in Zinck et al. (2023a). The erroneous elevation datasets where the interferometric cross-track location failed are filtered based on the quality flags provided by the ESA.~~

We applied the dynamic and static corrections mentioned in Zinck et al. (2023a)were applied to both the REMA strips and the CryoSat-2 elevationsdataset to bring all elevations into the samea consistent reference frame regardless of sea level variations. The, following the methodology described by Zinck et al. (2023a). For REMA, the corrected surface elevation (*h*)h_{corr}) was calculated as:

$$h_{corr} = h_{data} - \Delta h_{geoid} - \alpha(\Delta h_T + \Delta h_{MDT} + \Delta h_{IBE}) \quad (5)$$

where h_{data} is obtained based on the formula mentioned in Zinck et al. (2023a) as follows:

~~$h = h_{Data} - \Delta h_{Geoid} - \alpha(\Delta h_T + \Delta h_{MDT} + \Delta h_{IBE})$,~~ (5)

where $h_{Data}$the uncorrected surface elevation, Δh_{Geoid} is either the CryoSat-2 or REMA surface elevation above the WGS84 ellipsoid, Δh_{Geoid} is the EGM2008 the geoid offset from EGM2008 (Pavlis et al., 2012), $\Delta h_T$$\Delta h_T$ is the tidal height, Δh_{MDT} from the CATS2008_v2023 ocean tide model (6-hour intervals, ~3 km resolution), Δh_{MDT} is the mean dynamic topography, Δh_{IBE} from the DTU15MDT dataset (Andersen et al., 2015), and Δh_{IBE} is the inverse barometer effect, and the coefficient α ensures a smooth transition from grounded to floating ice (Shean et al., 2019), which increases from 0 to 1 with distance beyond the grounding line. The grounding line product of the ASAID was used to define α. The correction for the tides and the inverse barometer effect were based on 6-hourly NCEP/NCAR sea-level pressure residuals (Kalnay et al., 1996), referenced to a mean sea level pressure of 1013 hPa. Tidal and barometric corrections were applied based on the acquisition time of the first stereo image. The parameter settings for our experiment are the same as the settings mentioned in Zinck et al. (2023a). After this step, both the filtered REMA and CryoSat-2 elevation data are referenced to the EGM2008 geoid.

The double coregistration of the REMA strips was performed based on CryoSat-2 measurements. We have defined the criteria mentioned in Zinck et al. (2023a) that should be fulfilled before the coregistration of a REMA DSM in each DEM strip with CryoSat-2 data. To include smaller but good quality REMA strips to obtain a more complete time series of freeboard ice thickness, we set the latitude and longitude criteria for the CryoSat-2 distribution to be at least 5 km for both directions. We set the time gap between the acquisition date of CryoSat-2 and the REMA DSM strip to be. The stereo image pairs used to generate the DEMs are typically acquired within one month, as in Zinck et al. (2023a). Through trial and error, we reset the number of available CryoSat-2 measurementsa short time interval—usually within one month to be at least 75 to ensure that we performed a good plane fit and kept sufficient REMA strips. The residuals minutes to a few hours. Therefore, applying tidal and inverse barometric effect (IBE) corrections based on the acquisition time of the first image introduces only minimal temporal bias. The coefficient α ensures a smooth transition between the DEM stripsgrounded and the median DEM were usedfloating ice, varying from 0 to perform the plane fit.

To evaluate the accuracy of the REMA DSM strips, we used four REMA DSM strips1 with distance from 2019 to the floating ice edge to the grounding line (Shean et al., 2019), as defined by the ASAID product (Bindschadler et al., 2011a):

$$\alpha(l) = \begin{cases} 0, l \leq 0\text{km} \\ \frac{1}{3}, 0\text{km} < l \leq 3\text{km} \\ 1, l > 3\text{km} \end{cases} \quad (6)$$

The ASAID grounding line product serves as an input to the BURGEE framework and is the same dataset used in Zink et al. (2023a).

CryoSat-2 data were similarly corrected using the same tide model and additional fields from the Level 2 SARIn product (Howard et al., 2019; Zhang et al., 2020). Erroneous elevation measurements resulting from failed interferometric cross-track positioning were excluded based on quality flags provided by European Space Agency.

To identify and remove elevation outliers, we used the REMA 200 m mosaic DEM (Howat et al., 2019; 2022b) as a reference surface for both the REMA 2 m strips and the CryoSat-2 data. In regions of the PIIS where uncorrected REMA strips exhibited unrealistic elevation changes exceeding 30 m, we applied a more conservative threshold of 100 m elevation difference to exclude outliers.

Co-registration of REMA strips to CryoSat-2 followed a modified procedure from Zinck et al. (2023a), with the following criteria: 1) The longitudinal and latitudinal spacing between CryoSat-2 footprints must be at least 5 km to ensure uniform distribution within the REMA 2m strip data coverage; 2) The acquisition time interval between CryoSat-2 data and REMA strip data must not exceed one month to minimize elevation change impacts over time; and 3) A minimum of 75 valid CryoSat-2 data points must be distributed within the REMA strip coverage area to enable sufficient data for plane fitting and co-registration, thereby eliminating tilt and vertical bias in the REMA 2m strip DEM.

Residuals between each REMA strip and the CryoSat-2 data were used to apply tilt and vertical shift corrections through plane fitting. The final REMA strips are referenced to the EGM2008 geoid, ensuring both high internal consistency and improved absolute accuracy.

To assess the accuracy of the corrected REMA strips, we compared three strips from 2019–2021 with nearly contemporaneous ICESat-2 ~~elevations~~ATL06 data (Smith et al., ~~2024). Using points covered by the REMA DSM strips,~~2019; Smith et al., 2023). The ICESat-2 elevations were converted to heights relative to the instantaneous sea surface by referencing them to the EGM2008 geoid and applying corrections for ocean tides and the inverse barometer effect, following Wang et al. (2021). Processing steps see Figure 5. At overlapping locations between the datasets, we calculated the mean elevation difference ~~of the elevation of the (~~REMA ~~DSM strip~~ minus ~~the elevation of the~~ ICESat-2 ~~data was -1.14 m (~~) and the standard deviation of ~~2.85 m) over 7285 points in the December 23, 2019 scene, -2.64 m (standard deviation of 1.81 m) over 7837 points in the January 11, 2020 scene, -3.77 m (standard deviation of 2.56 m) over 802 points in the November 24, 2021 scene, and -1.93 m~~

~~(standard deviation of 2.54 m) over a total of 15924 points in four scenes (~~this bias. As shown in Table 2~~). The ~~, the corrected REMA strips exhibited lower standard deviations ~~of~~compared to the ~~elevation of~~uncorrected data, indicating reduced uncertainty. However, a consistent negative mean bias remained, with the corrected REMA ~~DSM strips were~~elevations appearing systematically lower than those from ICESat-2.

Table 2 The means and standard deviations of ~~**the**~~ uncorrected ~~**REMA DSM strips. From this comparison, we conclude that the uncertainties for our**~~and corrected REMA ~~**DSM strips is ±3 m (equivalent to ±24 m in floating ice thickness).**~~strip elevations minus the ICESat-2 elevation.

Date	Days Gap (day)	Data	Counts	Mean (m)	Standard deviation (m)
2019/12/23 2019/12/28	5	Uncorrected REMA ~~DEM~~strip	2335	-5.16	9.34
		Corrected REMA ~~DEM~~strip	7285	-1.14	2.85
2020/01/11 2020/01/09	2	Uncorrected REMA ~~DEM~~strip	6551	0.23	10.11
		Corrected REMA ~~DEM~~strip	7837	-2.64	1.81
2021/11/30 2021/11/24	6	Uncorrected REMA ~~DEM~~strip	827	0.76	5.99
		Corrected REMA ~~DEM~~strip	802	-3.77	2.56
Total		Uncorrected REMA ~~DEM~~strip	9713	-1.14	10.03
		Corrected REMA ~~DEM~~strip	15924	-1.93	2.54

~~**Table 2** The means and standard deviations of uncorrected and corrected REMA DEM strip elevations minus the ICESat-2 elevation~~

This bias likely results from the differing measurement principles of the two satellite systems: CryoSat-2 (used for REMA correction) operates in the Ku-band and can penetrate the upper snowpack, whereas ICESat-2 uses green laser altimetry, which reflects off the snow surface. As a result, CryoSat-2—and by extension, the corrected REMA strips—tend to report slightly lower surface elevations than ICESat-2, especially over snow-covered areas. Additional factors such as residual temporal offsets, snow accumulation variability, and surface roughness may also contribute. Based on this comparison, we estimate the uncertainty of the corrected REMA strips as −1.93 ± 2.54 m, equivalent to 15.44 ± 20.32 m in floating ice thickness.

Surface elevation changes over the PIIS were derived from the corrected REMA strips. Additionally, MODIS optical imagery from the Images of the Antarctic Ice Shelves Version 2 dataset (Scambos et al., 2022), with a spatial resolution of 250 m and spanning from 1 January 2001 to 23 October 2023, was used to identify changes in surface ridges.

2.3 Ice-equivalent freeboard thickness ~~**calculations, surface feature observations and climate data analysis**~~**calculation**

~~The~~To estimate changes in ice-equivalent freeboard thickness ~~and Eulerian thickness changes were~~near ice rumple L, we used both the corrected REMA strips and ICESat-2 data. Specifically, ICESat-2 tracks 965 and 1094, which pass through ice rumple L, were analysed. Ice-equivalent freeboard thickness (H_f) was calculated ~~through~~ using Equation (7), following the methods ~~provided in~~of Griggs and Bamber (2011) and Shean et al. (2019~~) based on our~~):

$$H_f = h_{corr}\left(\frac{\rho_{sw}}{\rho_{sw} - \rho_{is}}\right) - h_{FAC} \quad (7)$$

where h_{corr} is the corrected ~~REMA DSM 2 m strips, with an~~surface elevation, ρ_{is} is the ice density ~~of (~~917 kg/m^3~~,~~), ρ_{sw} is the seawater density ~~of (~~1027 kg/ m^3~~, and~~), h_{FAC} is the firn air content of ice equivalent (in meters ~~of ice equivalent)~~ derived from the NASA GSFC-FDM v1.2.1 dataset ~~at~~(Medley et al., 2022a; 2022b), with a 5-day temporal resolution spanning from 1 January ~~1,~~ 1980 to 30 June ~~30, 2022 (Medley et al.,~~ 2022~~).~~.

2.4 Rift propagation observation

Previous studies have suggested that such grounding may be linked to the formation of transverse rifts south of ice rumple L (Joughin et al., 2021), potentially contributing to calving events between 2015 and 2020. However, Joughin et al. (2021) also point out that due to the limitations in the clarity of Sentinel-1 IW SAR imagery hinder a definitive assessment of the connection between ephemeral grounding and rift formation. We used ~~optical imagery and DSMs to derive surface changes at the PIIS. Surface feature changes at the PIIS were derived from~~ Landsat ~~8~~ optical ~~imagery provided by the USGS Earth Explorer and MODIS optical imagery provided in the~~ images ~~of the Antarctic Ice Shelves Version 2 dataset (Scambos et al., 2022) at a spatial resolution of 250 m between 1 January 2001 and 23 October 2023. The surface elevation changes were derived from the corrected REMA DSMs.~~, specifically the panchromatic band with a 15m spatial resolution, to track the rift propagation history. We ~~used three month moving mean~~then compared these results with our grounding line data ~~from the Oceanic Niño Index (ONI)~~to better understand the interaction between ephemeral grounding and ~~year round monthly mean anomaly data from the Antarctic Oscillation (AAO) index from 2014 to 2023 provided by the Climate Prediction Center to analyze the driving factors behind the appearance of ephemeral grounding events.~~rift propagation.

3 Results

3.1 Changes in the ~~Double-differential Vertical Displacement~~

~~**Observations of**~~ **double-differential vertical displacement** ~~**in the ephemeral grounding zone are influenced by both oceanic tides and ice shelf thinning (Figure 4(a) and Movie S1). This displacement, ranging from −2 m to 2 m closely matching the double-differential tidal height (Figure 4(b)). Positive displacement anomalies correspond to high tidal phases, while negative anomalies correspond to low tidal phases. Figure 4(a) illustrates this relationship, showing the floating region where negative double-differential vertical displacement indicated in blue. Movie S1 provides a more complete visualization, showing both negative and positive displacement. The floating area (exhibiting both negative and positive anomalies) is enclosed by the 2011 grounding line, derived using the DInSAR method. Our results are consistent with Friedl et al. (2020), who found that DROT-derived grounding zones, indicating the landward limit of tidal flexure, were located seaward (up to ~2 km) of those derived from DInSAR. A near-zero vertical displacement signal was observed at ice rumple L from at least November 4, 2016, until the 2020 calving event (February 11, 2020), subsequently reappearing on October 21, 2021 (point out by red arrow in Figure 4(a) and marked as red circle in Figure 4(b)). Analysis of the ONI time series (Figure 4(c)) reveals three warm periods (2015-2016, 2019, and 2024) and four cold periods (2017, 2018, 2021, and 2022-2023). Concurrently, the AAO index (Figure 4(d)) shows two positive phases during the warm periods (2015-2016 and 2019) and four positive phases during the cold periods (2018, 2021,**~~

~~2022, and 2023). These coupled atmospheric and oceanic forcings modulate oceanic conditions (Huguenin et al., 2024) and, consequently, the ephemeral grounding behavior.~~

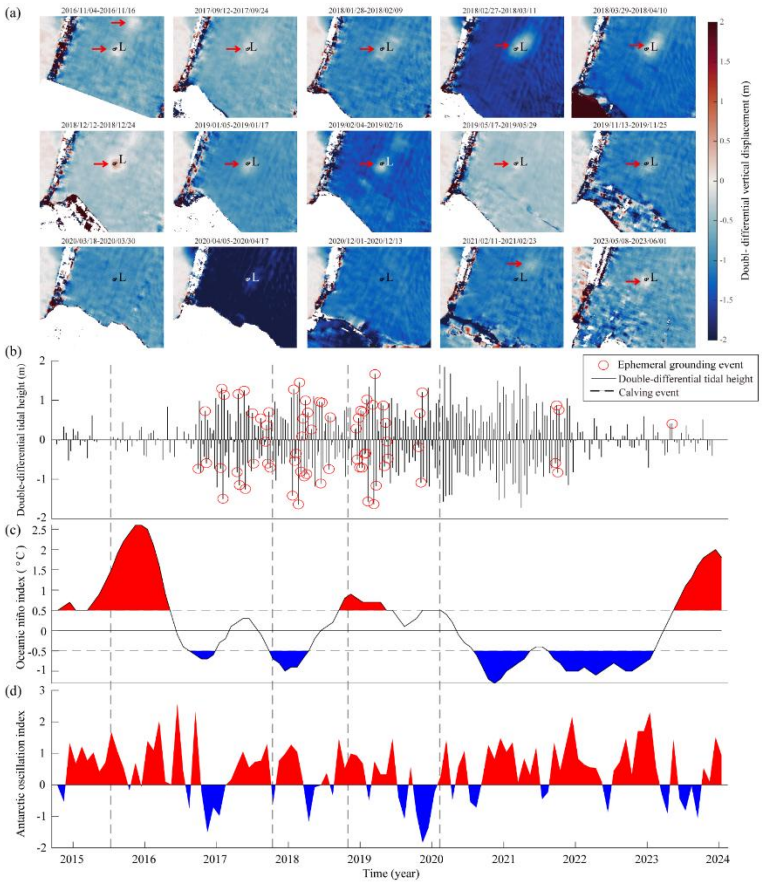

~~Figure 4. 2D~~Ephemeral grounding region, characterized by double-differential vertical displacements close to zero, shows significant correlation with oceanic tidal variations (Figures 6-7 and Movie S1). The tidal height difference was calculated from data extracted at a point near the ice rumple L (longitude 100.6149°W, latitude 75.1867°S), corresponding to the exact acquisition times of each Sentinel-1 image, which were at 4:35 AM on each date (Supplementary Table S1). One or two near-zero vertical displacement signals were detected at ice rumple L from at least November 2016 through April 2020, followed by a reappearance in December 2020. These signals are highlighted by yellow arrows in Figure 6a and marked by red vertical lines in Figure 6b. The reduced number of signals before August 2016 and after December 2021 likely reflects data limitations during periods when Sentinel-1B was not operational. Near-zero vertical displacement signals also occurred in 2016, 2017, and after the 2018 calving event. In December 2020, a similar signal appeared upstream of ice rumple L and progressively migrated toward the rumple, indicating that ephemeral grounding occurred as a thicker section of the ice shelf moved across the southern side of the sea ridge.

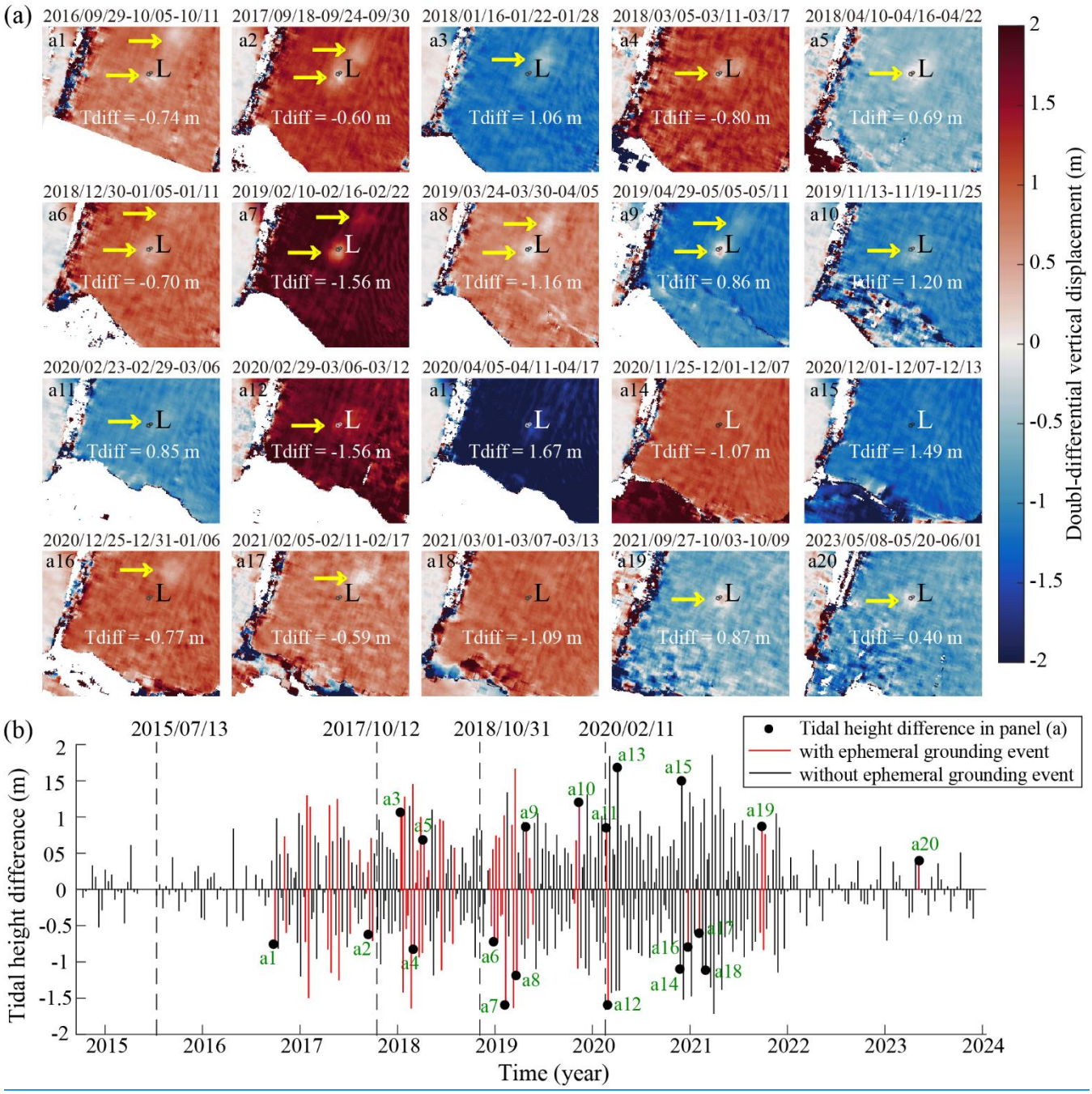

Figure 6. Two-dimensional double-differential vertical displacement changes, and time series of double-differential tidal height ~~difference changes, ONI changes, and AAO index changes~~differences. (a) ~~Examples~~Spatial distribution of ~~2D~~ double-differential vertical displacement changes ~~from~~between November 2016 ~~to~~and May 2023. ~~Red arrow point out the~~Yellow arrows highlight inferred ephemeral grounding ~~signal~~signals in each ~~result.~~displacement map. The tidal height difference (Tdiff) is labelled in each frame. (b) Time series of double-differential tidal height differences (black vertical lines) and inferred ephemeral grounding events (red ~~circles). Four dashed~~vertical lines ~~represent~~). Dashed lines indicate the timing of four major

calving events ~~in~~: 13 July ~~13,~~ 2015, ~~October~~ 12~~,~~ October 2017, ~~October~~ 31~~,~~ October 2018, and 11 February ~~11,~~ 2020. ~~(c) Time series of the ONI. Red parts~~

Figures 6a and 7a demonstrate that positive displacement anomalies generally correspond to negative tidal height differences (and vice versa), indicating an inverse linear relationship between these variables. However, Figure 7b reveals no clear correlation between tidal height and grounding region area, suggesting ephemeral grounding is not solely controlled by tidal forcing. Figure 7c shows 64 ephemeral grounding events from November 2016 to March 2021, with ~~values above 0.5°C indicate a warm period (El Niño), and blue parts~~35 occurring during neap tides and 29 during spring tides. From Figures 7c and 7d, it can be observed that larger grounded areas are evident during spring tides, when tidal amplitudes reach their maximum, while smaller grounded areas are observed during neap tides, when tidal heights are at their lowest. These patterns suggest that the variability in grounded area is reflecting the periodicity of tides. Together with ~~values below -0.5°C indicate a cold period (La Niña).~~Figure 6a, which shows the changes of the two near-zero vertical displacement signals, it suggests that thick ice advection from upstream may contribute to the grounding events. Therefore, ice dynamics likely play a significant role in the grounding process as well.

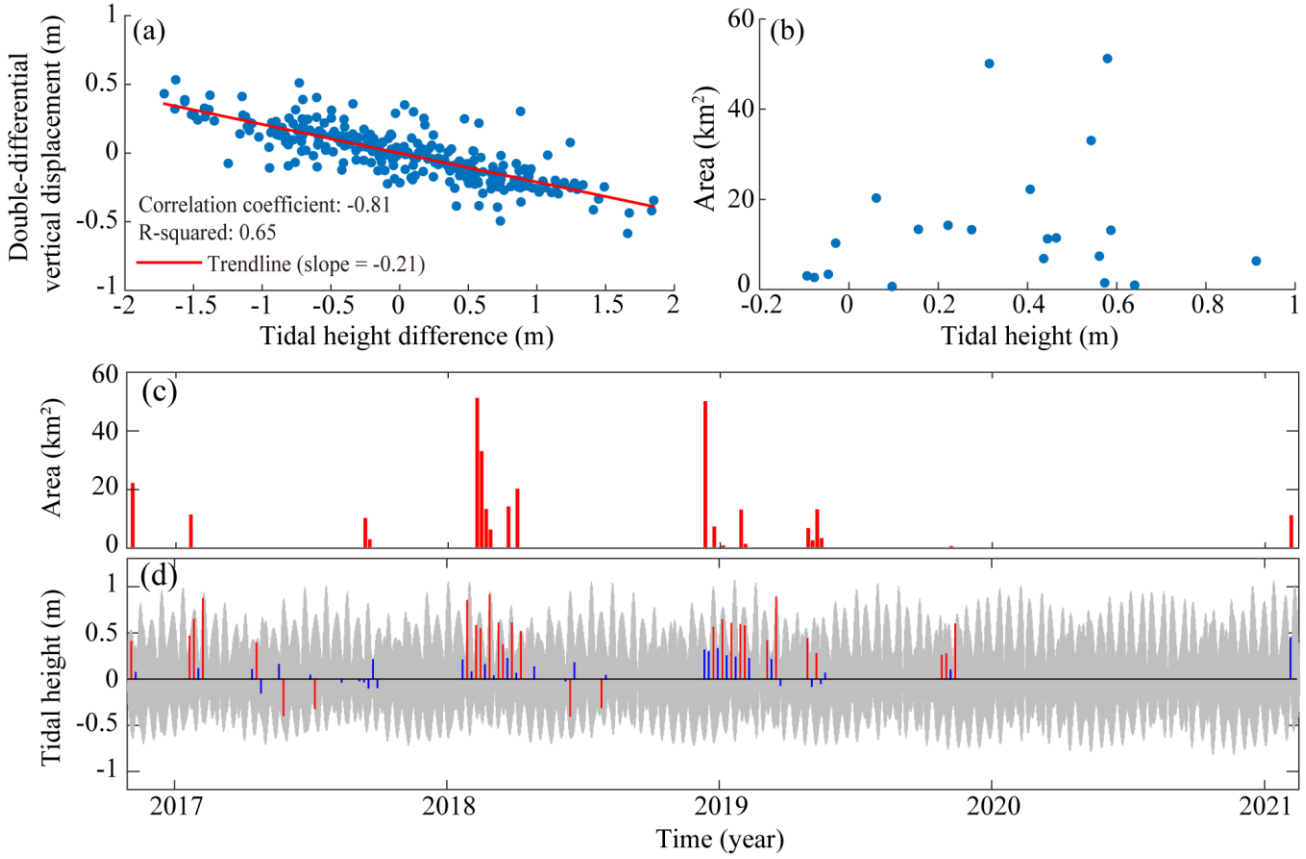

Figure 7. Comparison of tidal height differences with double-differential vertical displacement, comparison of tidal height differences and area of grounding region, including time series of area and tidal height variations. (a) Scatter plot of tidal height

difference versus double-differential vertical displacement, showing a strong negative linear correlation between the two variables (Pearson's r = –0.81, R^2 = 0.65, slope = –0.21). (b) Scatter plot of tidal height versus area of zero vertical displacement region, indicating no clear relationship between the two datasets. (c) Time series of changes in ice rumple area. (d) Time series of ~~the AAO index. The red parts with values above 0 indicate a positive phase, and the blue parts with values below~~ tidal height changes, where 0 ~~indicate a negative phase~~represents mean sea level. Blue vertical lines indicate ephemeral grounding events during the neap tide period, while red vertical lines represent those during the spring tide period.

3.2 Changes in surface features and ice thickness

~~The surface features observed from the MODIS images and surface elevations obtained from the corrected REMA DSM in Figure 5 show a surface ridge (~10 km long, ~2.5 km wide, which is circled by an ellipse in Figure 5) formed before December 2, 2010 and advected over the ice rumple L after October 2, 2014. Comparing the changes in surface features with the changes in surface elevation (Figure 6), we determined that the elevation of surface ridges passing through the ice rumple L after October 3, 2019 (<80m) was lower than that in 2015 (>80m). The number of surface ridges increased on October 3, 2019, compared with that before November 5, 2018.~~

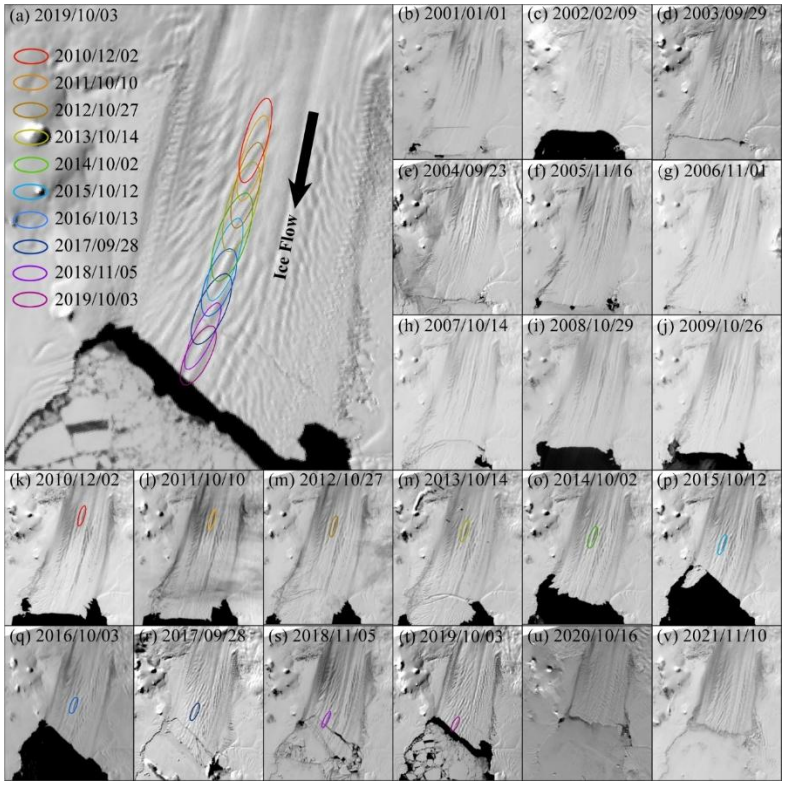

~~Figure 5.~~Figure 8 shows the evolution of the surface ridges' elevation and grounding areas using double-differential vertical displacement calculation (Section 2.1) from December 2010 to January 2021. Some ridges higher than 75 m were advected from upstream and passed through the area near the ice rumple L (Figure 8b-k). Near ice rumple L (red point in Figure 8), surface elevations remained around ~65 m between 2012–2017 and again during 2019–2020 (Figures 8d–h and 8j–k). The

highest elevation (~85 m) was recorded in 2018, while the lowest (~54 m) occurred in 2021. Between 2020 and 2021, surface elevation declined by ~10 m, equivalent to ~70 m of ice-equivalent freeboard thickness. The grounding line–enclosed area—corresponding to the region of zero vertical displacement—was largest in 2018 (Figure 8i).

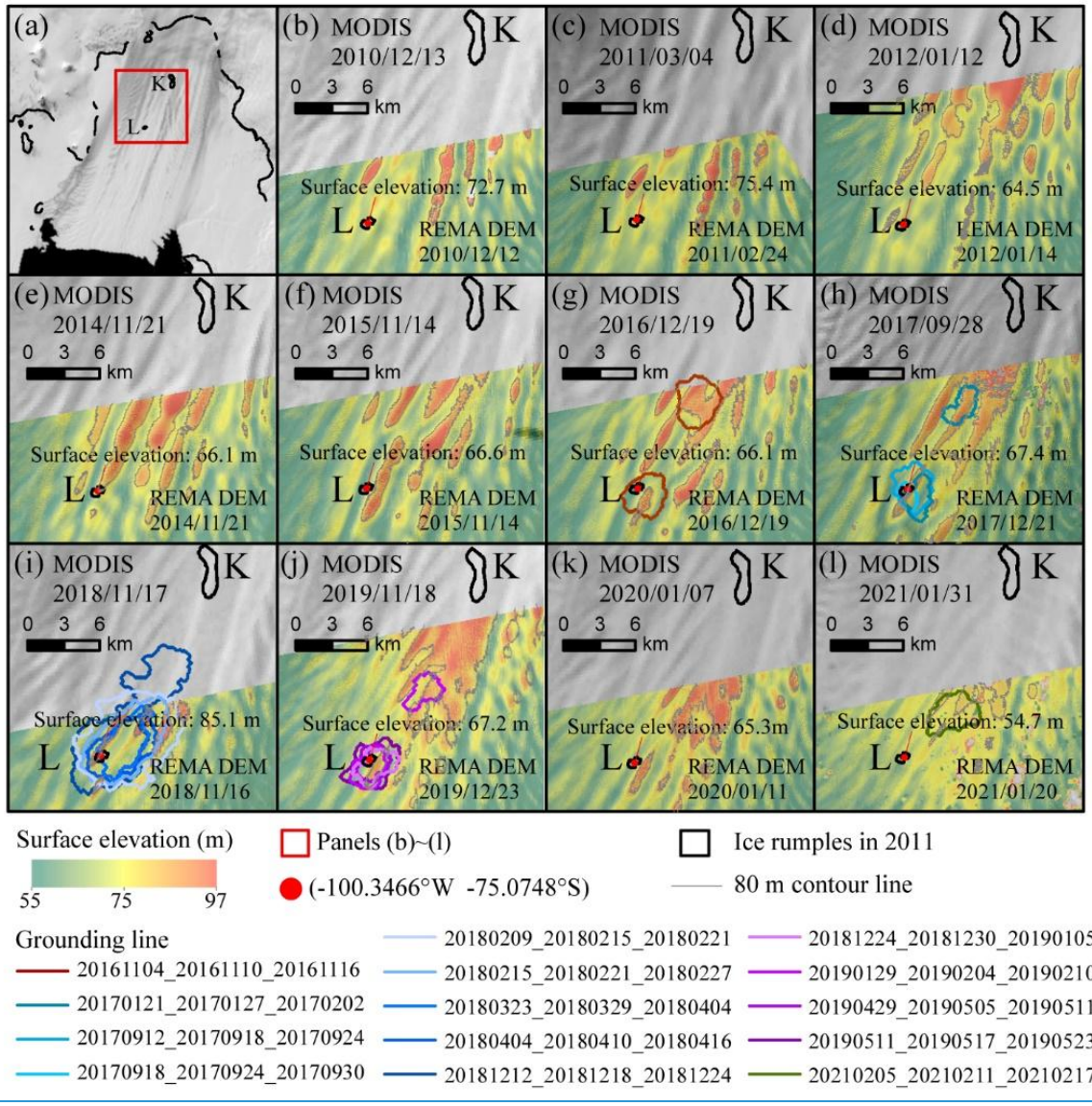

385 **Figure 8.** Changes in surface ridges at PIIS near ice rumple L. (a) Overview map showing the subregion outlined by the red frame, corresponding to panels (b) to (l). (b)–(l) Surface ~~ridge advects with ice flow between December 2, 2010 and October 3, 2019, and surface features change between January 2001 and November 2021. The ellipses with different colors circle a surface ridge that starts existing in (k) and continues advecting downstream. The background images are MODIS images between January 1, 2001 and October 3, 2019.~~

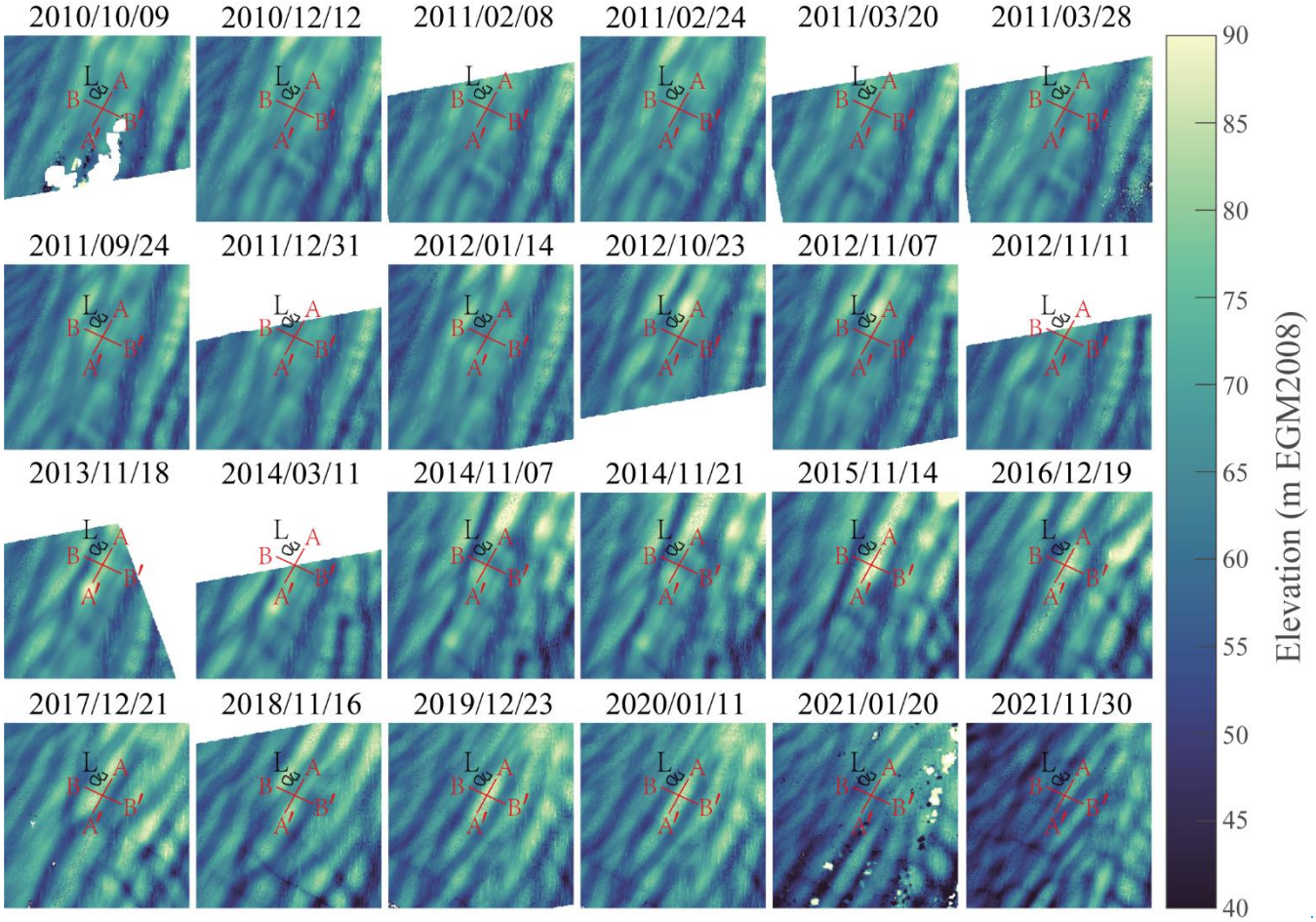

~~Figure 6.~~ ~~Surface elevation changes near the ice rumple L~~ ridges and their elevation changes from 2010 to 2021, derived from corrected REMA ~~DEMs. Lines AA' and BB' are used to extract the ice-equivalent freeboard thickness profiles in Figure 7.~~strips. The two black circles ~~represent~~ indicate the positions of ice rumples. Grounding lines are delineated based on the ~~2011 grounding lines~~zero-contour of the double-differential vertical displacement. Grey lines are the 80m contour line.

~~The ice-equivalent freeboard thickness profiles (Figure 7(a) (c)) provide evidence linking the observed double-differential vertical displacement signals to ephemeral grounding. Figure 7(a) and 7(b) illustrate the ice-equivalent freeboard thickness from 2010 to 2021 along longitudinal profile AA' and transverse profile BB', respectively. The surface elevation differences between December 12, 2010 and the other dates in Figure 7(c) reveal that the ridge on November 14, 2015 was approximately 35 m higher than on December 12, 2010, resulting in increased ice-equivalent freeboard thickness and regrounding of the ice shelf. However, after January 11, 2020, thinner ice advected over the submarine ridge (Figure 7(b)), as evidenced by the reduced surface elevation and the absence of contact between the ice shelf base and the ridge. This transition is consistent with the double-differential vertical displacement time series, where anomalies near ice rumple L diminished significantly after the 2020 calving event (February 11, 2020).~~

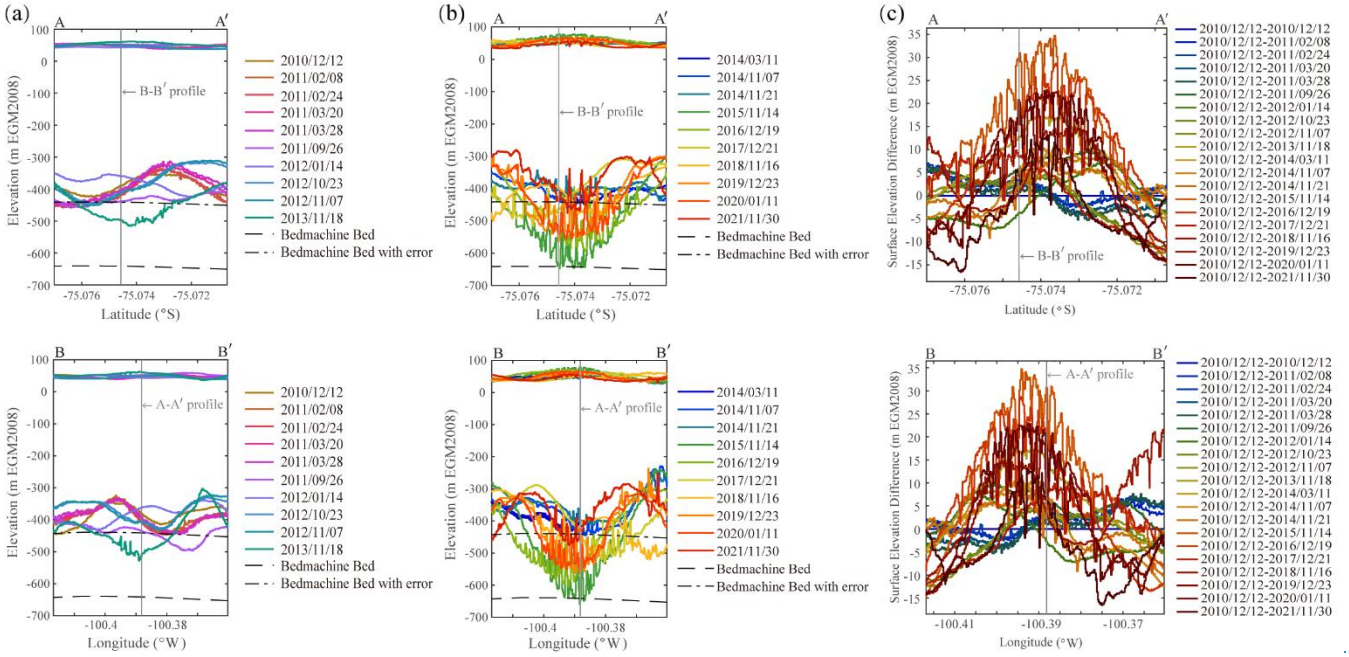

Figure 7. Ice-equivalent freeboard thickness and surface elevation profiles from 2010 to 2021. (a) Elevation profiles along lines AA' and BB' from December 2010 to November 2013. (b) Elevation profiles along line AA' and BB' from March 2014 to November 2021. (c) The surface elevation difference calculated from the surface elevation from other dates minus the elevation on 12 December 2010. The vertical gray line marks the intersection of profiles AA' and BB'. Dashed black lines in (a) and (b) show bed elevations from the BedMachine v3 dataset (Morlighem et al., 2020; Morlighem, 2022). Bed elevations, converted from EIGEN-6C4 to the EGM2008 geoid for consistency with REMA DSM strips, have an estimated error of 200 m.

Profiles of ice-equivalent freeboard thickness derived from ICESat-2 (Figure 9) link surface elevation and grounding area changes. ICESat-2 has three pairs of beams, each consisting of a strong and a weak beam. For our analysis of ice thickness changes, we selected two pairs of beams (gt2l, gt2r, gt3l, and gt3r) that pass through the ephemeral grounding region. The strong beams transmit with higher energy than the weak beams, and the weaker beams are positioned to the left of their paired strong beams. Thus, in our ICESat-2 data, 'gt2l' and 'gt3l' correspond to the weak beam positions, while 'gt2r' and 'gt3r' correspond to the strong beam positions (Figure 9a). Figure 9b shows mean thickness trends around the rumple along ICESat-2 tracks 965 and 1094 between 75.15°S and 75.05°S (Figure 9a). Track 965 reveals increasing ice thickness from 2015 to 2021, while track 1094 shows a decrease from 2015 to 2017, a rebound in 2018, and a decline after 2020. Bottom elevation profiles derived from ICESat-2 (Figures 9c-f) further reveal changes in grounding status. The ice shelf was ungrounded on 27 August 2020, 5 March 2021, and 25 May 2022, but showed weak grounding on 6 June 2020. Figures 9e and 9f suggest that the bed elevation beneath the rumple is likely too high in the BedMachine v3 dataset (red dashed line). Therefore, our results could help correct this potential error in the BedMachine v3 dataset. By integrating double-differential vertical displacement data with bottom elevation profiles, we find that ephemeral grounding signatures disappeared after March 2020 and reappeared in November 2020.

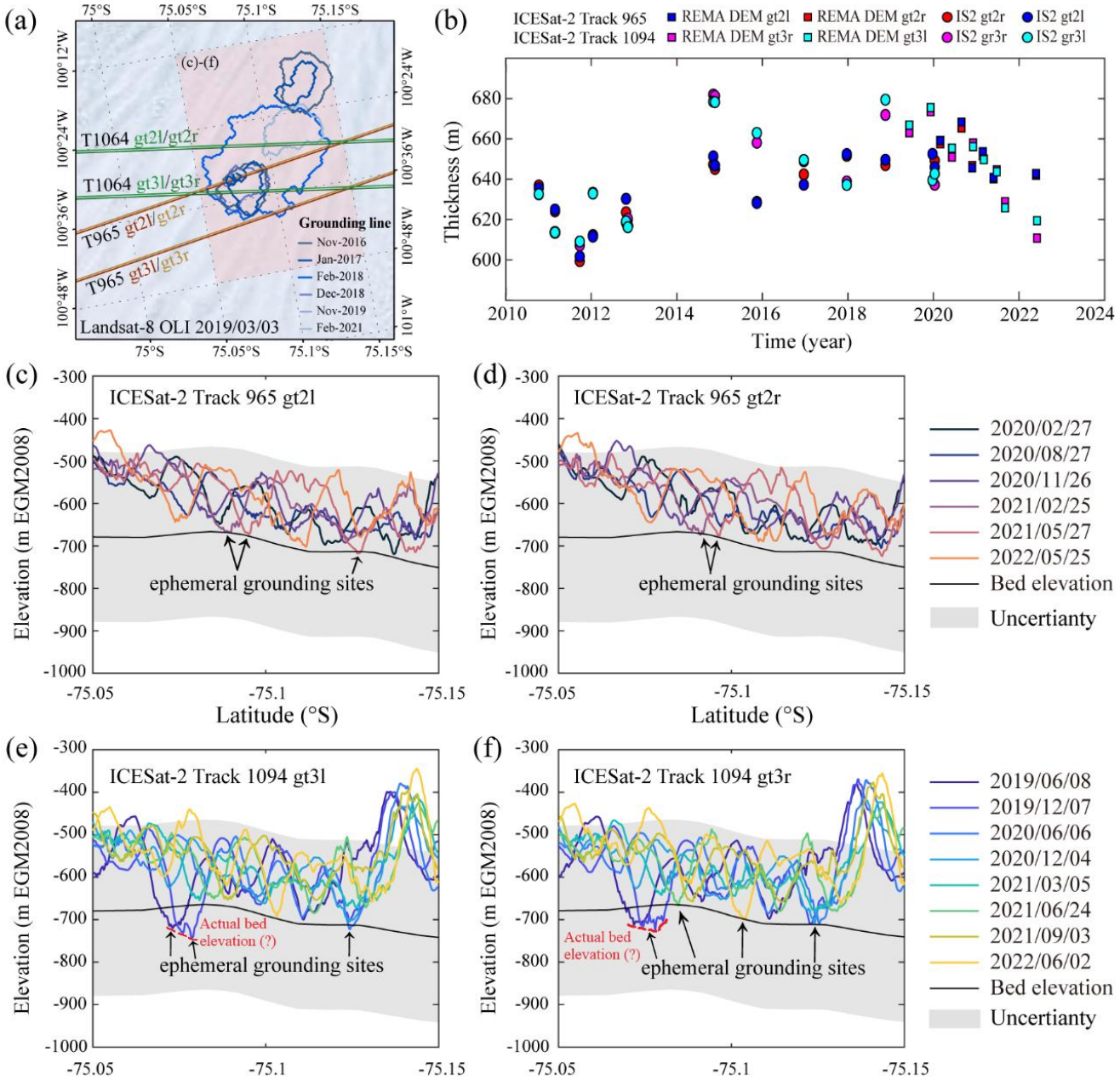

Figure 9. Time series of mean ice-equivalent freeboard thickness and ice shelf bottom elevation profiles along ICESat-2 tracks 965 and 1094. (a) ICESat-2 track 1094 and track 965 that used for ice-equivalent freeboard thickness change analysis and grounding lines near the ice rumple L from April 2011 to February 2021. Background is from Landdsat-8 OLI optic image on 3 March 2019. (b) Time series of mean ice-equivalent freeboard thickness (2010–2022). (c)–(d) Ice shelf bottom elevation profiles along ICESat-2 tracks 965 (gt2l and gt2r) between February 2020 and May 2022. (e)–(f) Ice shelf bottom elevation profiles along ICESat-2 tracks 1094 (gt3l and gt3r) between June 2019 and June 2022. Bed elevations are from the BedMachine v3 dataset (Morlighem et al., 2020; Morlighem, 2022), converted from EIGEN-6C4 to the EGM2008 geoid to match the

vertical datum of REMA strips. The estimated vertical uncertainty is ±200 m (shown as a grey transparent box). The potential actual bed elevation is marked by a red dashed line.

3.3 Rift propagation history from 2013 to 2019

Using Landsat images, we tracked the propagation history of the rifts from 2013 to 2019 (Figure 10). Rift R1 first appeared in the image from 15 December 2017 (Figure 10e), after the region passed through the ephemeral grounding zone, as seen in Figure 10c. Similarly, Rift R2 appeared in the 11 December 2018 image (Figure 10g), following its passage through the same grounding region. These two rifts ultimately led to the 2020 calving event. Therefore, our results suggest that ephemeral grounding events are linked to rift propagation, indirectly influencing the ice shelf calving process.

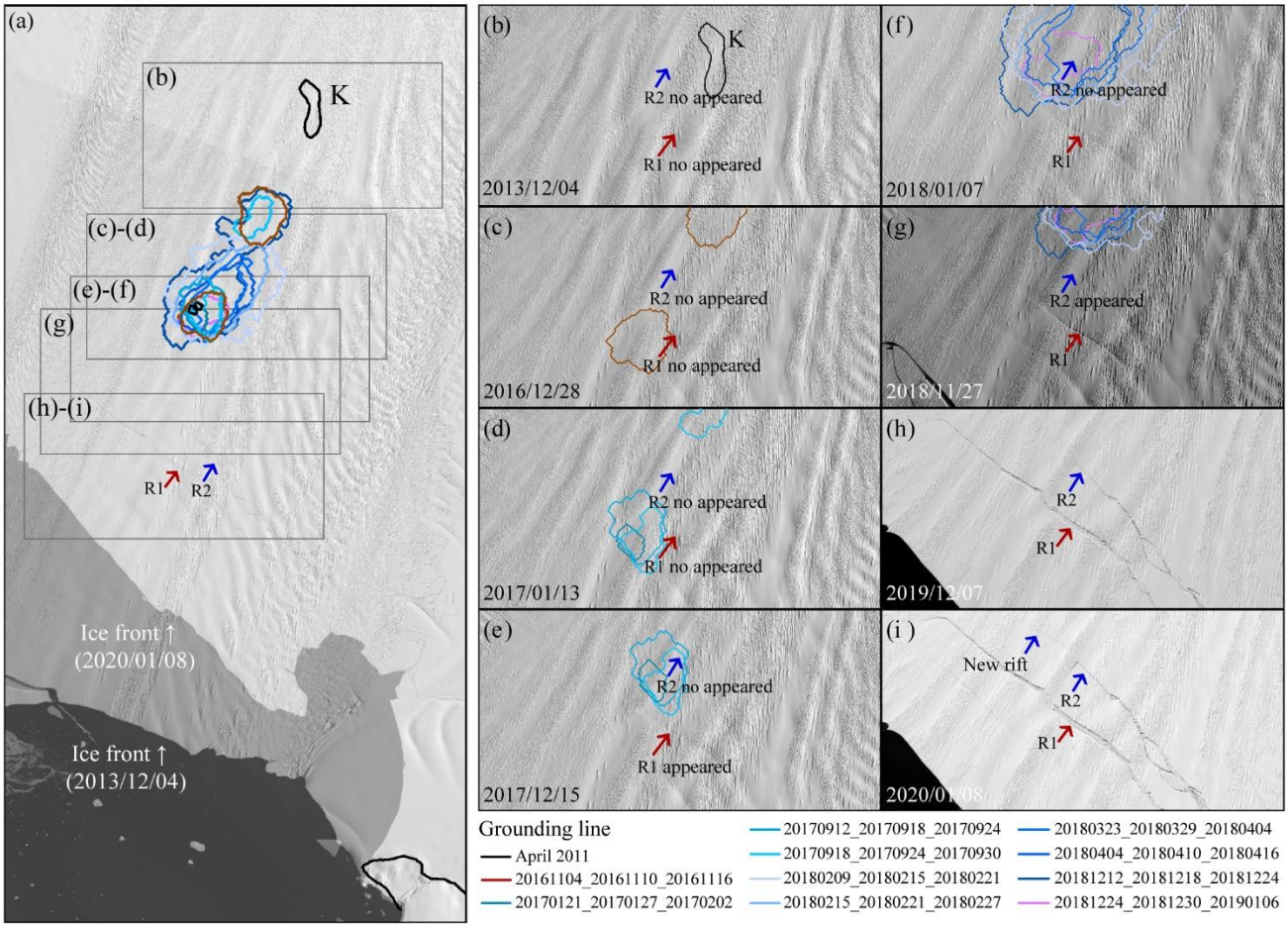

Figure 10. Rift propagation history from 2013 to 2019. (a) Overview map showing the positions of panels (b) to (i). The background image is a Landsat-8 panchromatic image from 8 January 2020, overlaid on another Landsat-8 panchromatic image from 4 December 2013, of Pine Island Glacier. (b)-(i) show the propagation history of the rifts R1 (red arrow) and R2 (blue arrow), which led to the 2020 calving event. The black circles indicate the positions of ice rumple K. Grounding lines are delineated based on the near-zero value of the double-differential vertical displacement.

4 Discussion

~~Tidal~~By integrating vertical displacement patterns, tidal height differences, and ICESat-2-derived ice thickness profiles, we captured ephemeral grounding of PIIS between 2014 and 2023. These findings emphasize the importance of combined geodetic and altimetric observations in resolving ephemeral grounding behaviour.

Our results reveal recurring of ephemeral grounding at ice rumple L from at least November 2016 through April 2020, followed by a reappearance in December 2020. This signal is modulated by tidal dynamics and variations in ice shelf thickness. Near-zero vertical displacement signals were observed during multiple years and were most prominent during spring tide periods when tidal amplitudes were highest. This finding supports the idea that tidal variations can modulate the vertical position of the ice shelf base, causing ~~sub-ice-shelf keels~~ it to intermittently contact the seafloor~~,~~ and resulting in ephemeral grounding (Minchew et al., 2017). ~~The vertical height~~The dual-satellite configuration significantly enhanced detection capabilities for ephemeral grounding events. When both Sentinel-1A and Sentinel-1B were operational, their combined 6-day repeat cycle increased the probability of capturing imagery during periods of large tidal variation, when ephemeral grounding is most readily observable. However, during single-satellite periods—before Sentinel-1B's launch in April 2016 and after its failure in January 2022—the extended 12-day repeat cycle of Sentinel-1A alone substantially reduced opportunities to coincide with optimal tidal conditions, hampering detection of these transient phenomena. This temporal sampling limitation underscores how the deployment of higher-resolution SAR satellites with improved revisit frequencies will enhance our ability to observe ephemeral grounding events, ultimately enabling the construction of denser, more temporally continuous records of grounding line dynamics. Our grounding line results also highlight that the DROT method can derive more detailed information than DInSAR at the fast-moving ice shelf, providing a valuable dataset for modelling input.

Thickness of ice advected from upstream has also observed to modulate the grounding of the rumple. Notably, the surface elevation peaked in 2018 and declined significantly between 2020 and 2021, coinciding with changes in grounding behaviour. Near-zero vertical displacement signals, indicative of ephemeral grounding, were detected at ice rumple L from November 2016 through April 2020. These signals disappeared during the 2020–2021 thinning period but reappeared in December 2020. In that instance, a similar signal emerged upstream of the rumple and gradually migrated toward it, suggesting that a thicker section of the ice shelf had moved over the sea ridge, re-establishing ephemeral contact with the bed. With time series of ephemeral grounding activities, the accurately derived ice draft elevations could be used to correct the bed elevation under the ephemeral grounding area, which ~~is~~ could be important to ice dynamics modelling study of PIG.

In summary, our study demonstrates that ephemeral grounding at ice rumple L is modulated by the interaction between tidal forcing, ice shelf thickness, and evolving sub-ice geometry. These results provide new insights into the mechanisms driving ephemeral grounding behaviour. Notably, we find the rift that caused the 2020 calving event appeared after pass through the ephemeral grounding region. Arndt et al. (2018) emphasized the importance of final pinning points in controlling calving line

orientation, raising the possibility that ice rumple L may have acted as a final pinning point after the 2015 calving event, thereby influencing rift propagation and subsequent calving. Previous studies (Sun and Gudmundsson, 2023; Joughin et al., 2021) have suggested that calving is the key process causing the speedup of PIG after 2017. These findings underscore the need for high-resolution ice shelf modelling to evaluate how ephemeral grounding affects stress redistribution and overall ice shelf stability.

De Rydt et al. (2014) demonstrated that both the height of the ridge and the gap between the ridge and the ice shelf strongly influence the inflow of warm bottom waters into the cavity, and consequently, the melt rate. The melt rate may influence the ice thickness near to the grounding line upstream than the ice rumples K and L. This process may have contributed to the ice thickness changes upstream and indirectly influenced the disappearance of ephemeral grounding signals following the 2020 calving event. We have added further analysis on the basal melt rate and ocean temperature in the Appendix A. Although smaller-scale basal channels and keel geometries are primarily shaped by melt-driven processes (Bindschadler et al., 2011b; Dutrieux et al., 2013; Stanton et al., 2013; Dutrieux et al., 2014b; Joughin et al., 2016), the lack of direct, high-temporal-resolution basal melt rate measurements after 2020 limits our ability to capture short-lived grounding events and confirm the role of ocean-driven melting. Future work should prioritize the integration of dense time series from new SAR missions and in situ oceanic data to better resolve ephemeral grounding behaviour and its implications for ice shelf evolution and calving dynamics in a warming climate.

5 Conclusion

This study presents the time series of ephemeral grounding events between 2014 and 2023 at the central PIIS, based on DROT applied to Sentinel-1 SAR data. By integrating double-differential vertical displacement maps, tidal height differences, and thickness data calculated from ~~the double-differential vertical displacement, can simply illustrate the ephemeral grounding location and grounding line location (Figure 4(a), Movie S1). The area changes of the 'spots' near the position L in Figure 4(a) regularly varies from time to time, supporting the evidence that corrugations with periodic spacing on the submarine ridge were caused by sub-ice-shelf keels with tidal modulation (Graham et al., 2013; Davies et al., 2017). Our results~~ surface elevation data from REMA strips and ICESat-2, we show that ephemeral grounding is modulated by the combined effects of tidal forcing, evolving sub-ice geometry, and changes in ice shelf thickness. Near-zero vertical displacement signals—indicative of intermittent grounding—were repeatedly observed throughout the study period, particularly as the grounded area expanded during spring tides with large tidal amplitudes. Changes in ice thickness also play an important role in driving ephemeral grounding at the PIIS.

We show that ice shelf thickening preceded grounding events, while thinning contributed to ungrounding. The presence and migration of near-zero displacement signals suggest that thicker ice flowing over topographic highs can cause ephemeral grounding. Observed large-scale surface and basal structures, including keels and channels, reflect the influence of inherited

bed topography, while smaller-scale geometries could shape by basal melt processes modulated by ocean temperature variability. We also show that the rifts responsible for the 2020 calving event appeared after the region passed through the ephemeral grounded area, suggesting that these ephemeral grounding events may have changed the stress distribution of the ice front and contributed to the formation of the rifts.

Our findings demonstrate the highly accurate remote-sensing techniques for monitoring grounding processes. The grounding lines derived from our DROT results can be scaled up to regional applications and provide critical boundary conditions for ice flow modelling efforts. We also reveal that ephemeral grounding influences stress redistribution, calving dynamics, and the long-term stability of vulnerable ice shelves of PIG. These observations could be used to validate the relevant processes in numerical modelling, which is currently poorly represented. In the future, improved satellite coverage, denser SAR time series, and in situ ocean measurements will provide comprehensive database to apply our method in deriving grounding line behaviours of much larger scale.

Appendix A. Oceanic condition changes and analysis

To address the oceanic condition changes, we extracted time series data on mean basal melt rates from 2010 to 2017 using the MEaSUREs ITS_LIVE Antarctic Quarterly 1920 m Ice Shelf Height Change and Basal Melt Rates v1 dataset (Paolo et al., 2023; 2024). This dataset offers quarterly basal melt rate estimates, with uncertainties, from 17 March 1992 to 16 December 2017, at a 1920 m spatial resolution. However, these estimates are based on surface elevation changes from radar altimetry and ice fluxes from the Glacier Energy and Mass Balance model, not direct observations. Additionally, it does not cover our primary observation period from 2020 to 2023.

To further investigate oceanic influences, we examined ocean temperature time series from the PIG-N (longitude 102.0987°W, latitude 74.8644°S) and PIG-S (longitude 102.1588°W, latitude 75.0546°S) mooring locations using mooring data (Zhou et al., 2024; 2025). These records span from 2016 to 2024 and capture temperature variations at depths of 300–700 meters below mean sea level. This pan-Antarctic mooring compilation contains data on temperature, salinity, and current velocity in the Southern Ocean (90°S–60°S) since 1975, with contributions from data centres, research institutes, and individual data owners (Zhou et al., 2024). ~~double-differential vertical displacement can rarely be observed in the ice rumple L after the 2020 calving event (Figure 4(b)). The~~ However, the moorings located in Pine Island Bay and not directly beneath the ice shelf, which limits their applicability to sub-shelf melting processes.

Profiles of ice-equivalent freeboard thickness ~~changes also prove that the deep keels no longer contacted the submarine ridge in 2020~~ (derived from ICESat-2 link surface elevation and grounding changes (Figure A). Figure Aa shows mean thickness trends around the rumple along ICESat-2 tracks 965 and 1094 between 75.15°S and 75.05°S (Figure 9b). Track 965 reveals

increasing ice thickness from 2015 to 2021, while track 1094 shows a decrease from 2015 to 2017, a rebound in 2018, and a decline after 2020.

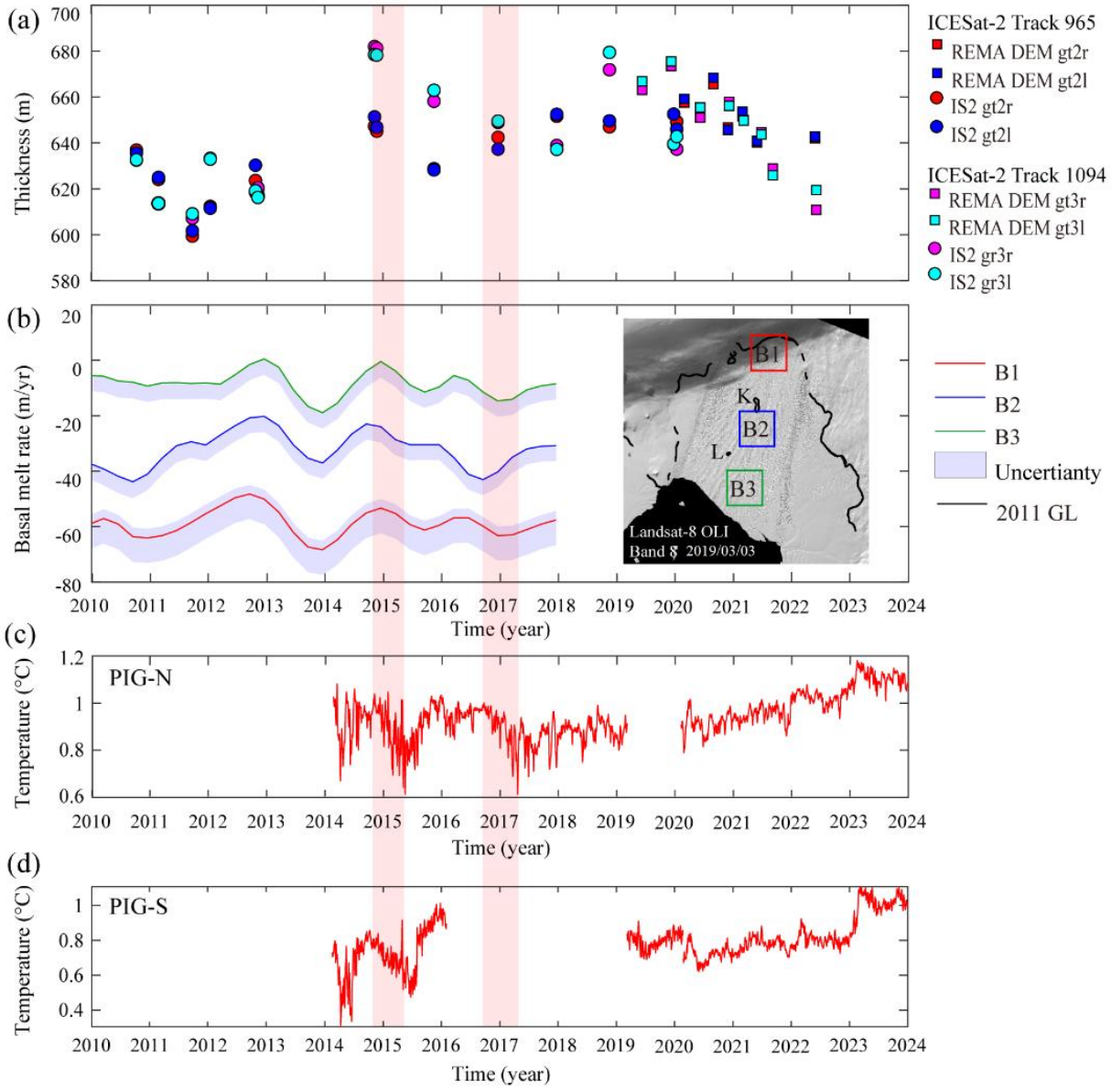

Figure ~~7(a)~(b)). Double-differential vertical displacement and~~ **A.** Time series of mean ice-equivalent freeboard thickness, basal melt rate, and ocean temperature. (a) Time series of mean ice-equivalent freeboard thickness (2010–2022). (b) Time series of mean basal melt rate (2010–2017), averaged across blocks B1, B2, and B3, extracted from the MEaSUREs ITS_LIVE Antarctic Quarterly 1920 m Ice Shelf Height Change and Basal Melt Rates v1 dataset (Paolo et al., 2024). ~~suggest that sub-ice-shelf keels remained grounded on the submarine ridge until the 2020 calving event. After calving, the ice shelf re-advanced, approaching the historical positions of the 2017 and 2018 calving fronts, which allowed for potential re-grounded of sub-ice-shelf keels~~(c)-(d) reveal time series of ocean temperature at the PIG-N and PIG-S mooring stations from 2014 to 2024.

The ~~formation of sub-~~basal melt rate time series show a decrease in melting around 2015, coinciding with a peak in ice-equivalent freeboard thickness at all three locations (B1–B3; Figure Ab). During the same period, ocean temperatures near 600 meters depth decreased at both the PIG-N and PIG-S mooring stations (Figures Ac and Ad). At B2, located between ice rumples L and K, the basal melt rate increased after 2015 but declined again after 2017 (Figures Aa and Ab). This decline corresponds with a drop in ocean temperature recorded at PIG-S (Figure Ad). However, from 2020 to 2023, ocean temperatures near 600 m depth at PIB showed a continuous increase, which could have contributed to enhanced basal melting of the ice shelf ~~keels~~during that time (Figures Ac and Ad).

Smaller-scale basal ~~channels has been attributed to~~channel and keel geometries are primarily shaped by melt-~~related~~driven processes~~, basal topography, and time-varying ice flow dynamics~~ (Bindschadler et al., ~~2011~~2011b; Dutrieux et al., 2013; Stanton et al., 2013; Dutrieux et al., ~~2014a~~2014b; Joughin et al., 2016). ~~The basal channel and basal keels form at a similar location (Figure 4), which is related to the bed topography. As the ice moves downstream of the grounding line, local surface elevations evolve as the ice approaches hydrostatic equilibrium (Shean, 2016). A local surface low/high in grounded ice indicates a topographic low/high in~~ Mooring observations from 2014 to 2024 reveal two distinct periods of ocean temperature decline around 2015 and 2017 (Figure Ac, d), during which basal melting near ice rumple L also decreased (Figure Ab). Following 2020, however, ocean temperatures began to rise again. Correspondingly, ice thickness time series (Figures Aa) show a substantial thinning of approximately 70 m. Although direct basal melt rate measurements are unavailable for this period, the ~~bed, forming surface troughs/ridges (Joughin et al., 2016). The bed topography near~~ observed warming at 600 m depth near PIB suggests that the ~~grounding line is W-shaped, with two troughs adjacent to the topographic high. These two troughs could allow thicker~~ ice ~~to be advected downstream over~~shelf base may have reached this depth, potentially enhancing basal melting. This increased melting would have further thinned the ice shelf, thereby widening the thickness gap between the ice base and the submarine ridge~~ and form surface ridges~~.

~~Melt related processes are also very important for the formation of sub ice shelf keels. Based on previous studies, mooring observations over the period from 2009 to 2020 indicate fluctuations in ocean temperature variability (Christianson et al, 2016; Joughin et al., 2021). From 2009 to 2017, the basal melt rate of the PIIS decreased (Paolo et al., 2023). From 2012 to 2014, atmospheric teleconnection caused by a La Niña event weakened CDW advection from the open ocean, cooled the PIB, and decreased basal melt rates (Thoma et al., 2008; Dutrieux et al., 2014b; St-Laurent et al., 2015; Christianson et al., 2016; Webber et al., 2017; Davis et al., 2018; Liu et al., 2024; Huguenin et al., 2024). This is because El Niño weakens coastal easterlies and enhances the cross-shelf transport of warm CDW, whereas La Niña allows stronger surface easterlies and increases the on-shelf flow of cold surface waters, which reduces the cross-shelf transport of warm CDW (Huguenin~~In summary, these data show periods of temperature decline around 2015 and 2017, which were accompanied by reduced ice thickness near ice rumple L, followed by warming after 2020 and a corresponding ice shelf thinning of approximately 70 meters. However, direct basal melt rate measurements are unavailable for the post-2020 period (Figure A). While the observed warming at 600 m depth near

PIB suggests increased basal melting that likely contributed to the thinning, variations in ocean temperature and basal melt rates alone cannot fully explain the observed changes in ice shelf thickness or influence the small-scale keels.

~~et al., 2024).~~ ~~Mooring observations revealed no evident changes in ocean temperature time series from 2017 to 2020 (Joughin et al., 2021). The meltwater flux from the PIG in 2020 was approximately half that in 2009 and equivalent to that in 2012 and 2014 (Yoon et al., 2022). Additionally, there was a significant decreasing trend in the wind speed and deep seawater temperature at depths ranging from 880 m to 1000 m near the ice front between 2015 and 2018 (Liu~~ ~~**et al., 2024).**~~ ~~The ONI time series indicates that a strong El Niño started in 2015, followed by two weak La Niña events in 2017 and 2018 and a weak El Niño event in 2019 (Figure 3(c)). In general, positive phases of the SAM are more likely to occur during La Niña, whereas negative phases occur more frequently during El Niño. However, two positive phase periods of the AAO appeared in 2015 and 2019 during the two El Niño events (Figure 3(d)). Huguenin et al. (2024) noted that the AAO tends to offset the ENSO warming effect and reduce the strength of the atmospheric teleconnection to the Amundsen Sea region. Combining the ONI and AAO time series with ocean conditions from 2015 to 2020, we can infer that basal melting was weak during the cold period from 2015 to 2020 and may have allowed thicker ice to advect farther downstream, causing ephemeral grounding at the submarine ridge until the 2020 calving event.~~

~~As mentioned by Bradley et al. (2022), when the ice front of the PIG retreated from the 2009 position to the 2020 position, melt rates within 10 km of the ice front increased significantly; the melt response to calving was sensitive to the thickness of the gap between the ice shelf and the seabed ridge. As shown by our ice thickness results (Figure 6(b)), the ice thickness decreased significantly between 11 January 2020 and 20 November 2021. This implies that the ice shelf becomes thinner and that the thickness gap between the ice shelf and the submarine ridge becomes larger, resulting in a higher basal melting rate. Because of the thinner ice thickness and the higher basal melting rate, the ephemeral grounding signals disappeared after the 2020 calving event.~~

~~Based on the time series surface changes in the PIIS, we agree with Joughin et al. (2021), who proposed that ephemeral grounding may be related to some of the transverse rifts that originated south of the ice rumple L and caused the four calving events that occurred between 2015 and 2020. However, the unclear pattern of newly formed rifts in SAR imagery limits the ability to investigate how ephemeral grounding influences rift formation. Furthermore, Arndt et al. (2018) reported that the final pinning points are important controls on the orientation of the calving line of the PIIS. We propose that the ephemeral grounding site at the central ice shelf may evolve into a final pinning point after the 2015 calving event and influenced rift propagation, which led to future ice shelf calving events in 2017, 2018, and 2020. Further studies on ice shelf modeling are needed to understand how the ephemeral grounding site on the central PIIS influences rift propagation.~~

~~5 Conclusions~~

~~This study used double-differential vertical displacement time series observations from Sentinel-1A/B imagery to identify a pattern in ephemeral grounding changes between October 2014 and December 2023. We found that the ephemeral grounding~~

~~site on the central ice shelf of the PIIS appeared until the 2020 calving event and after October 2021. The double-differential vertical displacement time series support the evidence that the periodically spaced corrugations on the submarine ridge are caused by sub-ice-shelf keels with tidal modulation. Based on our observations and previous studies, we conclude that the decrease in basal melting due to La Niña and the positive phase of AAO allowed thicker ice to move over the submarine ridge and cause ephemeral grounding. However, the 2020 calving event increased the basal melting rate outside of the submarine ridge and caused the ephemeral grounding to disappear. We conclude that calving and atmospheric forcing influence basal melting and indirectly influence ephemeral grounding. We propose that the ephemeral grounding site at the central ice shelf may evolve into a final pinning point and may influence future ice shelf calving events. Further studies on ice shelf modeling are needed to understand the interaction between ephemeral grounding and rift propagation.~~

***Code and sample availability*:** All codes and processed time series data used for analysis and plotting in this study are available from ~~Qian~~Chien et al. (2025a), including ice front positions delineated from Landsat panchromatic imagery and Sentinel-1 SAR imagery based on Google Earth Engine, double-differential vertical displacement, ~~and~~ corrected REMA ~~DSM~~ strips, and MODIs images for Figure 8. The zenodo link provided in ~~Qian~~Chien et al. (2025a) will be made public after acceptance of the paper. The grounding lines extracted from the double-differential vertical displacement map are available in the supplementary material of this study. The Sentinel-1 image IDs and ephemeral area can be accessed in Supplementary Tables S1 and S2. Reviewers can access the code and datasets through the link below:

https://zenodo.org/records/15844913?token=eyJhbGciOiJIUzUxMiJ9.eyJpZCI6ImY5MTY3ZGI4LTZmYWQtNDcwOS05ZmFiLTQyMTU4YzVhMjRhZSIsImRhdGEiOnt9LCJyYW5kb20iOiI4YmQ2MTY2Nzg4ZTUyYzNhYWZiYmMyZDQ4MDg1NmM1ZSJ9.VNGqgibhOoN5KN39EhcRyTK3Ras3T79O83lszsJ0ag05foJxtk3BK63HlGGoKT6-XCSHBwmcMB046GqCYPS4NQ

Data availability: All software (except GAMMA, which is commercial software and was used to generate displacement in slant-range direction), codes, and satellite and climate datasets used in this study are publicly available and can be obtained from the following sources: The MATLAB plotting codes on which this article is based are available in Greene et al (2017) and Greene et al. (2021). The BURGEE codes for corrected REMA ~~DSM~~ strips are available in Zinck et al. (2023b). The tidal model driver based on MATLAB code is available in Greene et al. (2023). Sentinel-1 images are available for free download from the Alaska Satellite Facility website at https://asf.alaska.edu/. Processed MODIS images are available in Scambos et al. (2022). BedMachine version 3 dataset is from Morlighem (2022). REMA ~~DSM~~ 200 m DEM mosaic and REMA ~~DSM~~ 2 m DEM strips are available from Howat et al. (2022a) and Howat et al. (2022b), respectively. CryoSat Baseline-D SARIn Level 2 data are available on the ESA CryoSat Science Server at https://science-pds.cryosat.esa.int/#Cry0Sat2_data%2FIce_Baseline_D%2FSIR_SIN_L2. ICEsat-2 Level 2 ATL06 product is available from Smith et al. (2023). ~~Ground~~ASAID grounding line products are available from Bindschadler et al. (2011a), Rignot et al. (2016), ~~Floricioiu et al. (2021),~~ and ~~Mohajerani~~this study (Chien et al. ~~(2021.~~, 2025a). Firn air content is available from Medley et al. (~~2022). Single~~2022b). 6-hourly NCEP/NCAR sea-level ~~hourly ERA5 data~~pressure is tagged in Google Earth Engine (NCEP_RE_sea_level_pressure). Basal melt rate product can be accessed from ~~1940 to present are available from Hersbach~~Paolo et al. ~~(2023.~~, (2024). The ~~Oceanic Niño Index~~ocean temperature time series at the PIG-N and ~~the Antarctic Oscillation Index are~~PIG-S mooring locations is available ~~from~~and regularly updated in NetCDF format via the ~~National Oceanic and Atmospheric Administration (NOAA) Climate Prediction Center~~SEANOE database at https://~~origin.cpc.ncep.noaa.gov/products/analysis_monitoring/ensostuff/ ONI_v5.php and https://www.cpc.ncep.noaa.gov/p~~doi.org/10.17882/99922 (Zhou et al., 2024). ~~roducts/precip/CWlink/daily_ao_index/aao/monthly.aao.index.b79.current.ascii, respectively.~~

Video supplement: Movie S1 "Double-differential vertical displacement changes from November 2014 to November 2023 at the PIIS" can be accessed at the zenodo link ~~provide~~provided by ~~Qian~~Chien et al. (2025b).

Author contribution: ~~YQ~~YC, CZ, and ~~CZ~~SS designed the experiments and ~~YQ~~YC carried them out. ~~YQ~~YC developed the MATLAB code and performed all the experiments. BZ ~~provide~~provided the corrected CryoSat-2 dataset. ~~YQ~~YC prepared the manuscript with contributions from all co-authors.

Competing interests: The contact author has declared that none of the authors has any competing interests.

Acknowledgements: This research is funded by the National Natural Science Foundation of China (41941010 and 42171133) and the Fundamental Research Funds for the Central Universities (2042024kf0016). We thank all the organizations or projects listed in Open Research. We thank the anonymous reviewers and editors for their insightful comments to improve the manuscript. We sincerely thank Anne Solgaard and Anders Kusk for providing helpful suggestions related to SAR image post-processing. We sincerely thank Jan Wuite for providing helpful suggestions related to tidal correction. We sincerely thank Hilmar Gudmundsson for providing helpful suggestions related to the ephemeral grounding change analysis.

Financial support: This research is funded by the National Natural Science Foundation of China (42171133 and 41941010 ~~and 42171133~~) and the Fundamental Research Funds for the Central Universities (2042024kf0016).

References

~~Alley, R. B., Anandakrishnan, S., Christianson, K., Horgan, H. J., Muto, A., Parizek, B. R., Pollard, D., and Walker, R. T.: Oceanic forcing of ice sheet retreat: West Antarctica and more, Annu. Rev. Earth Planet. Sci., 43, 207–231, https://doi.org/10.1146/annurev-earth-060614-105344, 2015.~~

Andersen, O., Knudsen, P., Stenseng, L.: The DTU13 MSS (Mean Sea Surface) and MDT (Mean Dynamic Topography) from 20 Years of Satellite Altimetry. In: Jin, S., Barzaghi, R. (eds) IGFS 2014. International Association of Geodesy Symposia, vol 144. Springer, Cham. https://doi.org/10.1007/1345_2015_182, 2015

Arndt, J. E., Larter, R. D., Friedl, P., Gohl, K., Höppner, K., and the Science Team of Expedition PS104: Bathymetric controls on calving processes at Pine Island Glacier, The Cryosphere, 12, 2039–2050, https://doi.org/10.5194/tc-12-2039-2018, 2018.

Bamber, J. L., Westaway, R. M., Marzeion, B., and Wouters, B.: The land ice contribution to sea level during the satellite era, Environ. Res. Lett., 13, 063008, https://doi.org/10.1088/1748-9326/aac2f0, 2018.

Benn, DI, Luckman, A, Åström, JA, Crawford, AJ, Cornford, SL, Bevan, SL, Zwinger, T, Gladstone, R, Alley, K, Pettit, E & Bassis, J, 'Rapid fragmentation of Thwaites Eastern Ice Shelf', The Cryosphere, vol. 16, no. 6, pp. 2545-2564. https://doi.org/10.5194/tc-16-2545-2022, 2022. Bindschadler, R., Choi, H., Wichlacz, A., Bingham, R., Bohlander, J., Brunt, K., et al.: Getting around Antarctica: new high-resolution mappings of the grounded and freely-floating boundaries of the Antarctic ice sheet created for the International Polar Year, The Cryosphere, 5, 569–588, https://doi.org/10.5194/tc-5-569-2011, 2011a.

Bindschadler, R. A., Vaughan, D. G., and Vornberger, P.: Variability of basal melt beneath the Pine Island Glacier ice shelf, West Antarctica, J. Glaciol., 57, 581–595, https://doi.org/10.3189/002214311797409802, ~~2011~~2011b.

Boncori, M. J. P., Andersen, M. L., Dall, J., Kusk, A., Martijn, K., Bech Andersen, S., et al.: Intercomparison and validation of SAR-based ice velocity measurement techniques within the Greenland ice sheet cci project, Remote Sens., 10, 929, https://doi.org/10.3390/rs10060929, 2018.

Bradley, A. T., Bett, D. T., Dutrieux, P., De Rydt, J., and Holland, P. R.: The influence of Pine Island Ice Shelf calving on basal melting, J. Geophys. Res. Oceans, 127, e2022JC018621, https://doi.org/10.1029/2022JC018621, 2022.

Chen, Y., Zhou, C., Ai, S., Liang, Q., Zheng, L., Liu, R., and Lei, H.: Dynamics of Dålk glacier in east Antarctica derived from multisource satellite observations since 2000, Remote Sens., 12, 1809, https://doi.org/10.3390/rs12111809, 2020.

Chien, Y. D.: Dataset for the paper "Ephemeral grounding on the Pine Island Ice Shelf, West Antarctica, from 2014 to 2023", Version 5, Zenodo, https://zenodo.org/records/15844913, 2025a.

Chien, Y. D.: Double-differential vertical displacement changes from November 2014 to November 2023 at the Pine Island Ice Shelf., Version 1, Zenodo, https://zenodo.org/records/14843806, 2025b.

Christianson, K., Bushuk, M., Dutrieux, P., Parizek, B. R., Joughin, I. R., Alley, R. B., et al.: Sensitivity of Pine Island Glacier to observed ocean forcing, Geophys. Res. Lett., 43, 10817–10825, https://doi.org/10.1002/2016GL070500, 2016.

Corr H. F. J., Doake C. S. M., Jenkins A., Vaughan D. G.: Investigations of an "ice plain" in the mouth of Pine Island Glacier, Antarctica. Journal of Glaciology, 47(156), 51-57. doi:10.3189/172756501781832395, 2001.

Davies, D., Bingham, R. G., Graham, A. G. C., Spagnolo, M., Dutrieux, P., Vaughan, D. G., et al.: High-resolution subb-ice-shelf seafloor records of twentieth century ungrounding and retreat of Pine Island Glacier, West Antarctica, J. Geophys. Res. Earth Surf., 122, 1698–1714, https://doi.org/10.1002/2017JF004311, 2017.

Davis, P. E. D., Jenkins, A., Nicholls, K. W., Brennan, P. V., Abrahamsen, E. P., Heywood, K.Depoorter, M., Bamber, J., Griggs, J., Lenaerts, J. T. M., Ligtenberg, S. R. M., van den Broeke, M. R., et al.: Variability in: Calving fluxes and basal melt rates of Antarctic ice shelves. Nature, 502, 89–92. https://doi.org/10.1038/nature12567, 2013

De Rydt, J., P. R. Holland, P. Dutrieux, and A. Jenkins, Geometric and oceanographic controls on melting beneath Pine Island Ice Shelf on weekly to monthly timescales, J.Glacier, J. Geophys. Res. Oceans, 123, 8655–8669, https://doi.org/10.1029/2018JC014464, 2018119, 2420–2438, doi:10.1002/2013JC009513, 2014.

Dutrieux, P., Vaughan, D. G., Corr, H. F. J., Jenkins, A., Holland, P. R., Joughin, I., and Fleming, A. H.: Pine Island glacier ice shelf melt distributed at kilometre scales, The Cryosphere, 7, 1543–1555, https://doi.org/10.5194/tc-7-1543-2013, 2013.

Floricioiu, D., Krieger, L., Chowdhury, T. A., and Bässler, M.: ESA Antarctic Ice Sheet Climate Change Initiative (Antarctic_Ice_Sheet_cci): Grounding line location for key glaciers, Antarctica, 1994–2020, Version 2, ERC EDS Centre for Environmental Data Analysis, https://catalogue.ceda.ac.uk/uuid/7b3bddd5af4945c2ac508a6d25537f0a/, 2021.

Dutrieux, P., Rydt, J. D., Jenkins, A., Holland, P. R., Ha, H. K., Lee, S. H., et al.: Strong sensitivity of pine island ice-shelf melting to climatic variability, Science, 343, 174–178, https://doi.org/10.1126/science.1244341, 2014a.

Dutrieux, P., Stewart, C., Jenkins, A., Nicholls, K. W., Corr, H. F. J., Rignot, E., and Steffen, K.: Basal terraces on melting ice shelves, Geophys. Res. Lett., 41, 5506–5513, https://doi.org/10.1002/2014GL060618, 2014b.

Fricker, H. A., and Padman, L.: Ice shelf grounding zone structure from ICESat laser altimetry, Geophys. Res. Lett., 33, L15502, https://doi.org/10.1029/2006GL026907, 2006.

Fricker, H. A., ~~Fried, M. J., Hulbe, C. L., and Fahnestock, M. A.: Grounding-line dynamics and margin lakes, Ann. Glaciol., 55, 87–96, https://doi.org/10.3189/2014AoG66A216, 2014.~~

Galton-Fenzi, B. K., Walker, C. C., Freer, B. I. D., Padman, L., & DeConto, R. Antarctica in 2025: Drivers of deep uncertainty in projected ice loss. Science, 387(6734), 601–609. https://doi.org/10.1126/science.adt9619, 2025.

Friedl, P., Weiser, F., Fluhrer, A., and Braun, M. H.: Remote sensing of glacier and ice sheet grounding lines: A review, Earth-Sci. Rev., 201, 102948, https://doi.org/10.1016/j.earscirev.2019.102948, 2020.

Fürst, J., Durand, G., Gillet-Chaulet, F., Tavard, L., Rankl, M., Braun, M., and Gagliardini, O.: The safety band of Antarctic ice shelves, Nat. Clim. Change, 6, 479–482, https://doi.org/10.1038/nclimate2912, 2016.

Graham, A. G. C., Dutrieux, P., Vaughan, D. G., Nitsche, F. O., Gyllencreutz, R., Greenwood, S. L., et al.: Seabed corrugations beneath an Antarctic ice shelf revealed by autonomous underwater vehicle survey: Origin and implications for the history of pine island glacier, J. Geophys. Res. Earth Surf., 118, 1356–1366, 2013

Greene, C. A., Gwyther, D. E., and Blankenship, D. D.: Antarctic mapping tools for MATLAB, Comput. Geosci., 104, 151–157, https://doi.org/10.1016/j.cageo.2016.08.003, 2017.

Greene, C. A.: Antarctic Mapping Tools, Version 6, [Software], GitHub, https://github.com/chadagreene/Antarctic-Mapping-Tools, 2021.

Greene, C. A., Erofeeva, S., Padman, L., Howard, S., Sutterley, T., and Egbert, G.: The Tide Model Driver for MATLAB, Version 3.0, [Software], https://github.com/chadagreene/Tide-Model-Driver, 2023.

Griggs, J. A. and Bamber, J. L.: Antarctic ice-shelf thickness from satellite radar altimetry, J. Glaciol., 57, 485–498, https://doi.org/10.3189/002214311796905659, 2011.

Gudmundsson, G. H., Paolo, F. S., and Adusumilli, S., Fricker, H. A.: Instantaneous Antarctic ice sheet mass loss driven by thinning ice shelves, Geophys. Res. Lett., 46, 13903–13909, https://doi.org/10.1029/2019GL085027, 2019.

Hersbach, H., Bell, B., Berrisford, P., Biavati, G., Horányi, A., Muñoz Sabater, et al.: ERA5 hourly data on single levels from 1940 to present, Version 1, [Dataset], Copernicus Climate Change Service (C3S) Climate Data Store (CDS). https://doi.org/10.24381/cds.adbb2d47, 2023.

Hillenbrand, C. D., Smith, J. A., Hodell, D. A., Greaves, M., Poole, C. R., Kender, S., et al.: West Antarctic ice sheet retreat driven by Holocene warm water incursions, Nature, 547, 43–48, https://doi.org/10.1038/nature22995, 2017.

Hogg, A. E.: Locating Ice Sheet Grounding Lines Using Satellite Radar Interferometry and Altimetry, PhD Thesis, University of Leeds, 152 pp., https://etheses.whiterose.ac.uk/11356/, 2015.

Howard, S. L., Greene, C. A., Padman, L., Erofeeva, S., & Sutterley, T. CATS2008_v2023: Circum-Antarctic Tidal Simulation 2008, Version 2023, [Dataset], U.S. Antarctic Program (USAP) Data Center, https://doi.org/10.15784/601772., 2024

Howat, I., Porter, C., Smith, B. E., Noh, M. J., and Morin, P.: The reference elevation model of Antarctica, The Cryosphere, 13, 665–674, https://doi.org/10.5194/tc-13-665-2019, 2019.

Howat, I., Porter, C., Noh, M., Husby, E., Khuvis, S., Danish, E., et al.: The Reference Elevation Model of Antarctica – Strips, Version 4.1, [Dataset], Harvard Dataverse, https://data.pgc.umn.edu/elev/dem/setsm/REMA/strips/s2s041/2m/s76w101/, 2022a.

Howat, I., Porter, C., Noh, M., Husby, E., Khuvis, S., Danish, E., et al.: The Reference Elevation Model of Antarctica – Mosaics, Version 1.1, [Dataset], Harvard Dataverse, https://data.pgc.umn.edu/elev/dem/setsm/REMA/mosaic/v1.1/200m/, 2022b.

~~Huguenin, M. F., Holmes, R. M., Spence, P., and England, M. H.: Subsurface warming of the West Antarctic continental shelf linked to El Niño-Southern Oscillation, Geophys. Res. Lett., 51, e2023GL104518, https://doi.org/10.1029/2023GL104518, 2024.~~

Jacobs, S. S., Jenkins, A., Giulivi, C. F., and Dutrieux, P.: Stronger ocean circulation and increased melting under pine island glacier ice shelf, Nat. Geosci., 4, 519–523, https://doi.org/10.1038/ngeo1188, 2011.

Jenkins, A., Dutrieux, P., Jacobs, S. S., McPhail, S. D., Perrett, J. R., Webb, A. T., and David, W.: Observations beneath pine island glacier in west Antarctica and implications for its retreat, Nat. Geosci., 3, 468–472, https://doi.org/10.1038/ngeo890, 2010.

Jeong, S., Howat, I. M., and Bassis, J. N.: Accelerated ice shelf rifting and retreat at pine island glacier, west Antarctica, Geophys. Res. Lett., 43, 11720–11725, https://doi.org/10.1002/2016GL071360, 2016.

Joughin, I., Smith, B. E., and Abdalati, W.: Glaciological advances made with interferometric synthetic aperture radar, J. Glaciol., 56, 1026–1042, https://doi.org/10.3189/002214311796406158, 2010.

Joughin, I., Shean, D. E., Smith, B. E., and Dutrieux, P.: Grounding line variability and subglacial lake drainage on pine island glacier, Antarctica, Geophys. Res. Lett., 43, 9093–9102, https://doi.org/10.1002/2016GL070259, 2016.

Joughin, I., Shapero, D., Smith, B., Dutrieux, P., and Barham, M.: Ice-shelf retreat drives recent pine island glacier speedup, Sci. Adv., 7, eabg3080, https://doi.org/10.1126/sciadv.abg3080, 2021.

~~Lemos, A., Shepherd, A., McMillan~~Kalnay, E., Kanamitsu, M., Kistler, R., Collins, W., Deaven, D., Gandin, L., et al.: The NCEP/NCAR 40-Year Reanalysis Project. Bulletin of the American Meteorological Society, 77(3), 437-472, 1996 https://doi.org/10.1175/1520-0477(1996)077<0437:TNYRP>2.0.CO;2

Lhermitte, S., Sun, S., Shuman, C., Wouters, B., Pattyn, F., Wuite, J., et al.: Damage accelerates ice shelf instability and mass loss in Amundsen Sea Embayment. Proceedings of the National Academy of Sciences, 117(40), 24735-24741, 2020

Lowery, K., Dutrieux, P., Holland, P. R., Hogg, A. ~~E., Hatton,~~ E., ~~and Joughin, I.: Ice velocity of Jakobshavn Isbræ, Petermann~~ Gourmelen, N., and Wallis, B. J.: Spatio-temporal melt and basal channel evolution on Pine Island Glacier~~, Nioghalvfjerdsfjorden, and Zachariæ Isstrøm, 2015–2017,~~ ice shelf from ~~Sentinel-1A/B SAR imagery, The Cryosphere, 12, 2087–2097,~~CryoSat-2, EGUsphere [preprint], https://doi.org/10.5194/~~tc-12-2087-2018, 2018~~egusphere-2025-267, 2025.

~~Lei, Y., Gardner, A., and Agram, P.: Autonomous repeat image feature tracking (autorift) and its application for tracking ice displacement, Remote Sens., 13, 749, https://doi.org/10.3390/rs13040749, 2021.~~

~~Liu, M., Wang, Z., Zhang, B., Song, X., and An, J.: The variation in basal channels and basal melt rates of Pine Island Ice Shelf, Acta Oceanol. Sin., 43, 22–34, https://doi.org/10.1007/s13131-023-2271-x, 2024.~~

Marsh, O. J., Rack, W., Floricioiu, D., Golledge, N. R., and Lawson, W.: Tidally induced velocity variations of the Beardmore Glacier, Antarctica, and their representation in satellite measurements of ice velocity, The Cryosphere, 7, 1375–1384, https://doi.org/10.5194/tc-7-1375-2013, 2013.

Matsuoka, K., Hindmarsh, R., Moholdt, G., Bentley, M., Pritchard, H., Brown, J., et al.: Antarctic ice rises and rumples: Their properties and significance for ice-sheet dynamics and evolution. Earth-Science Reviews, 150, 724-745. https://doi.org/10.1016/j.earscirev.2015.09.004, 2015.

Medley, B., Neumann, T. A., Zwally, H. J., Smith, B. E., and Stevens, C. M.: Simulations of firn processes over the Greenland and Antarctic ice sheets: 1980–2021, The Cryosphere, 16, 3971–4011, https://doi.org/10.5194/tc-16-3971-2022, 2022a.

Medley, B., Neumann, T. A., Zwally, H. J., Smith, B. E., and Stevens, C. M.: NASA GSFC Firn Densification Model version 1.2.1 (GSFC-FDMv1.2.1) for the Greenland and Antarctic Ice Sheets: 1980–2022, Version 1.2.1, [Dataset], Zenodo, https://zenodo.org/records/7221954, 2022b.

Meloni, M., Bouffard, J., Parrinello, T., Dawson, G., Garnier, F., Helm, V., et al.: CryoSat Ice Baseline-D Validation and Evolutions, The Cryosphere, 14, 1889–1907, https://doi.org/10.5194/tc-14-1889-2020, 2020.

Miles, B. W. J. and Bingham, R. G.: Progressive unanchoring of Antarctic ice shelves since 1973, Nature, 626, 785–791, https://doi.org/10.1038/s41586-024-07049-0, 2024.

Milillo, P., Rignot, E., Mouginot, J., Scheuchl, B., Morlighem, M., Li, X., and Salzer, J. T.: On the short-term grounding zone dynamics of Pine Island Glacier, West Antarctica, observed with COSMO-SkyMed interferometric data, Geophys. Res. Lett., 44, 10436, https://doi.org/10.1002/2017GL074811, 2017.

~~Milillo, P., Rignot, E., Rizzoli, P., Scheuchl, B., Mouginot, J., Bueso-Bello, J., and Prats-Iraola, P.: Heterogeneous retreat and ice melt of Thwaites Glacier, West Antarctica, Sci. Adv., 5, aau3433, https://doi.org/10.1126/sciadv.aau3433, 2019.~~

Minchew, B. M., Simons, M., Riel, B., and Milillo, P.: Tidally induced variations in vertical and horizontal motion on Rutford ice stream, west Antarctica, inferred from remotely sensed observations, J. Geophys. Res. Earth Surf., 122, 167–190, https://doi.org/10.1002/2016JF003971, 2017.

~~Mohajerani, Y., Jeong, S., Scheuchl, B., Velicogna, I., Rignot, E., and Milillo, P.: Automatic delineation of glacier grounding lines in differential interferometric synthetic-aperture radar data using deep learning, Sci. Rep., 11, 4992, https://doi.org/10.1038/s41598-021-84309-3, 2021.~~

Morlighem, M., Rignot, E., Binder, T., Blankenship, D., Drews, R., Eagles, G., et al.: Deep glacial troughs and stabilizing ridges unveiled beneath the margins of the Antarctic ice sheet, Nat. Geosci., 13, 132–137, https://doi.org/10.1038/s41561-019-0510-8, 2020.

Morlighem, M.: MEaSUREs BedMachine Antarctica, Version 3, [Dataset], NASA National Snow and Ice Data Center Distributed Active Archive Center, https://nsidc.org/data/nsidc-0756/versions/3, 2022.

Mouginot, J., Rignot, E., & Scheuchl, B.: Sustained increase in ice discharge from the Amundsen Sea Embayment, West Antarctica, from 1973 to 2013. Geophysical Research Letters, 41, 1576–1584. https://doi.org/10.1002/2013GL059069, 2014

Otsu, N. A threshold selection method from gray-level histograms. IEEE Transactions on Systems, Man, and Cybernetics, 9(1), 62–66. https://doi.org/10.1109/TSMC.1979.4310076, 1979

Paolo, F. S., Fricker, H. A., & Padman, L.: Volume loss from Antarctic ice shelves is accelerating. Science, 348(6232), 327–331. https://doi.org/10.1126/science.aaa0940, 2015

Paolo, F. S., Gardner, A. S., Greene, C. A., Nilsson, J., Schodlok, M. P., Schlegel, N.-J., and Fricker, H. A.: Widespread slowdown in thinning rates of West Antarctic ice shelves, The Cryosphere, 17, 3409–3433, https://doi.org/10.5194/tc-17-3409-2023, 2023.

~~Paul, F., Bolch, T., Kääb,~~Paolo, F., Gardner, A. S., Greene, C. A. & Schlegel, N: MEaSUREs ITS_LIVE Antarctic Quarterly 1920 m Ice Shelf Height Change and Basal Melt Rates, 1992-2017, Version 1, [Data Set], NASA National Snow and Ice Data Center Distributed Active Archive Center, https://nsidc.org/data/nsidc-0792/versions/1, 2024.

~~A.,~~ ~~Nagler, T., Nuth, C., Scharrer, K., et al.: The glaciers climate change initiative: Methods for creating glacier area, elevation change and velocity products, Remote Sens. Environ., 162, 408–426, https://doi.org/10.1016/j.rse.2013.07.043, 2015.~~

Pavlis, N. K., Holmes, S. A., Kenyon, S. C., and Factor, J. K.: The development and evaluation of the Earth Gravitational Model 2008 (EGM2008), J. Geophys. Res., 117, B04406, https://doi.org/10.1029/2011JB008916, 2012.

Pritchard, H. D., Ligtenberg, S. R. M., Fricker, H. A., Vaughan, D. G., van den Broeke, M. R., and Padman, L.: Antarctic ice-sheet loss driven by basal melting of ice shelves, Nature, 484, 502–505, https://doi.org/10.1038/nature10968, 2012.

Qi, M., Liu, Y., Liu, J., Cheng, X., Lin, Y., Feng, Q., et al.: A 15-year circum-Antarctic iceberg calving dataset derived from continuous satellite observations, Earth Syst. Sci. Data, 13, 4583–4601, https://doi.org/10.5194/essd-13-4583-2021, 2021.

~~Qian, Y. D.: Dataset for the paper "Ephemeral grounding on the Pine Island Ice Shelf, West Antarctica, from 2014 to 2023", Version 5, Zenodo, https://doi.org/10.5281/zenodo.13357909, 2025a.~~

~~Qian, Y. D.: Double-differential vertical displacement changes from November 2014 to November 2023 at the Pine Island Ice Shelf., Version 1, Zenodo, https://zenodo.org/records/14843806, 2025b.~~

Rignot, E.: Fast Recession of a West Antarctic Glacier, Science, 281, 549–551, https://doi.org/10.1126/science.281.5376.549, 1998.

Rignot, E.: Ice-shelf changes in pine island bay, Antarctica, 1947–2000, J. Glaciol., 48, 247–256, https://doi.org/10.3189/172756502781831386, 2002.

Rignot, E., ~~Casassa, G., Gogineni, P., Krabill, W., Rivera, A., and Thomas, R.: Accelerated ice discharge from the Antarctic Peninsula following the collapse of Larsen B Ice Shelf, Geophys. Res. Lett., 31, L18401, https://doi.org/10.1029/2004GL020697, 2004.~~

~~Rignot, E.,~~ Mouginot, J., Morlighem, M., Seroussi, H., and Scheuchl, B.: Widespread, rapid grounding line retreat of Pine Island, Thwaites, Smith, and Kohler Glaciers, West Antarctica, from 1992 to 2011, Geophys. Res. Lett., 41, 3502–3509, https://doi.org/10.1002/2014GL060140, 2014.

Rignot, E., Mouginot, J., and Scheuchl, B.: Measures Antarctic grounding line from differential satellite radar interferometry, Version 2, [Dataset], NASA National Snow and Ice Data Center Distributed Active Archive Center, https://nsidc.org/data/NSIDC-0498/versions/2, 2016.

~~Rott, H., Rack, W., Skvarca, P., and De Angelis, H.: Northern Larsen Ice Shelf, Antarctica: Further retreat after collapse, Ann. Glaciol., 34, 277–282, 2002.~~

~~Rott, H., Abdel Jaber, W., Wuite~~Rignot, E., Mouginot, J., Scheuchl, B., ~~Scheiblauer, S., Floricioiu, D., van~~Van Den Broeke, M., Van Wessem, M. J., & Morlighem, M.: Four decades~~ M., et al.: Changing pattern~~ of ~~ice flow and~~Antarctic Ice Sheet mass

balance ~~for glaciers discharging into~~from 1979–2017. Proceedings of the ~~Larsen A and B embayments, Antarctic Peninsula, 2011 to 2016, The Cryosphere, 12, 1273–1291,~~National Academy of Sciences, 116(4), 1095–1103. https://doi.org/10.~~5194/tc-12-1273-2018, 2018.~~1073/pnas.1812883116, 2019

Sánchez-Gámez, P. and Navarro, F. J.: Glacier surface velocity retrieval using D-InSAR and offset tracking techniques applied to ascending and descending passes of sentinel-1 data for southern Ellesmere ice caps, Canadian Arctic, Remote Sens., 9, 442, https://doi.org/10.3390/rs9050442, 2017.

Scambos, T., Wallin, B., and Bohlander, J.: Images of Antarctic Ice Shelves, Version 2, [Dataset], NASA National Snow and Ice Data Center Distributed Active Archive Center, https://nsidc.org/data/nsidc-0102/versions/2, 2022.

Schmeltz, M., Rignot, E., and MacAyeal, D. R.: Ephemeral grounding as a signal of ice-shelf change, J. Glaciol., 47, 71–77, https://doi.org/10.3189/172756501781832502, 2001.

~~Scheuchl, B., Mouginot, J., Rignot, E., Morlighem, M., and Khazendar, A.: Grounding line retreat of Pope, Smith, and Kohler Glaciers, West Antarctica, measured with Sentinel 1a radar interferometry data, Geophys. Res. Lett., 43, 8572–8579, https://doi.org/10.1002/2016GL069287, 2016.~~

Shean, D. E.: Quantifying ice-shelf basal melt and ice-stream dynamics using high-resolution DEM and GPS time series, PhD Thesis, University of Washington, 2016.

Shean, D. E., Joughin, I. R., Dutrieux, P., Smith, B. E., and Berthier, E.: Ice shelf basal melt rates from a high-resolution digital elevation model (DEM) record for pine island glacier, Antarctica, The Cryosphere, 13, 2633–2656, https://doi.org/10.5194/tc-13-2633-2019, 2019.

Shepherd, A., Ivins, E. R., Geruo, A., Barletta, V. R., Bentley, M. J., Bettadpur, S., et al.: A reconciled estimate of ice-sheet mass balance, Science, 338, 1183–1189, https://doi.org/10.1126/science.1228102, 2012.

Shepherd, A., Fricker, H. A., & Farrell, S. L.: Trends and connections across the Antarctic cryosphere. Nature, 558, 223–232. https://doi.org/10.1038/s41586-018-0171-6, 2018.

Smith, J. A., Andersen, T. J., Shortt, M., Gaffney, A. M., Truffer, M., Stanton, T. P., et al.: Subb-ice-shelf sediments record history of twentieth-century retreat of pine island glacier, Nature, 541, 77–80, https://doi.org/10.1038/nature20136, 2017.

Smith, B., Fricker, H. A., Holschuh, N., Gardner, A. S., Adusumilli, S., Brunt, K. M., et al.: Land ice height-retrieval algorithm for NASA's ICESat-2 photon-counting laser altimeter. Remote Sensing of Environment, 233, 111352. https://doi.org/10.1016/j.rse.2019.111352, 2019

Smith, B., Fricker, H. A., Gardner, A. S., Medley, B., Nilsson, J., Paolo, F. S., et al.: Pervasive ice sheet mass loss reflects competing ocean and atmosphere processes, Science, 368, 1239–1242, https://doi.org/10.1126/science.aaz5845, 2020.

Smith, B., Adusumilli, S., Csathó, B. M., Felikson, D., Fricker, H. A., Gardner, A., Holschuh, N., et al.: ATLAS/ICESat-2 L3A Land Ice Height, Version 6, [Dataset], NASA National Snow and Ice Data Center Distributed Active Archive Center, https://doi.org/10.5067/ATLAS/ATL06.006, 2023.

Solgaard, A., Kusk, A., Merryman Boncori, J. P., Dall, J., Mankoff, K. D., Ahlstrøm, A. P., et al.: Greenland ice velocity maps from the PROMICE project, Earth Syst. Sci. Data, 13, 3491–3512, https://doi.org/10.5194/essd-13-3491-2021, 2021.

Stanton, T. P., Shaw, W. J., Truffer, M., Corr, H. F. J., Peters, L. E., Riverman, K. L., et al.: Channelized ice melting in the ocean boundary layer beneath Pine Island Glacier, Antarctica, Science, 341, 1236–1239, https://doi.org/10.1126/science.1239373, 2013.

Sun S, Gudmundsson GH. The speedup of Pine Island Ice Shelf between 2017 and 2020: revaluating the importance of ice damage. Journal of Glaciology. 2023;69(278):1983-1991. doi:10.1017/jog.2023.76

Wang, S., Alexander, P. M., Alley, R. B., ~~Still, H. and Hulbe, C.: Mechanics and dynamics of pinning points on the Shirase Coast, West Antarctica, The Cryosphere, 15, 2647–2665, https://doi.org/10.5194/tc-15-2647-2021, 2021.~~

~~Still, H., Campbell,~~Huang, Z., Parizek, B. R., Willet, A. G., & Anandakrishnan, S. Recent variability in fracture characteristics and ice flow of Thwaites Ice Shelf, West Antarctica. *Journal of Geophysical Research: Earth Surface*, 130, e2024JF008118, https://doi.org/10.1029/2024JF008118, 2025.

Walker, C.C., Millstein, J.D., Miles, B.W.J. ~~A., and Hulbe, C.: Mechanical analysis of pinning points in the Ross Ice Shelf, Antarctica, Ann. Glaciol., 60, 32–41, https://doi.org/10.1017/aog.2018.31, 2019.~~

~~St-Laurent, P., Klinck, J. M., and Dinniman, M. S.: Impact of local winter cooling on the melt of pine island glacier, Antarctica, J. Geophys. Res. Oceans, 120, 6718–6732, https://doi.org/10.1002/2015JC010709, 2015.~~

~~Strozzi, T., Luckman, A., Murray, T., Wegmüller, U., and Werner, C.: Glacier motion estimation using sar offset-tracking procedures, IEEE Trans. Geosci. Remote Sens., 40, 2384–2391, https://doi.org/10.1109/TGRS.2002.805079, 2002.~~

~~Thoma, M., Jenkins, A., Holland, D., and Jacobs, S.: Modelling Circum-Polar Deep-water intrusions on the Amundsen Sea continental shelf, Antarctica, Geophys. Res. Lett., 35, L18602, https://doi.org/10.1029/2008GL034939, 2008.~~

~~Webber, B. G. M., Heywood, K., J., Stevens, D. P., Dutrieux, P., Abrahamsen, E. P., Jenkins, A., et al.: Mechanisms driving variability in the ocean forcing of pine island glaciers,~~. Multi-decadal collapse of East Antarctica's Conger–Glenzer Ice Shelf. Nat. Geosci. ~~Commun., 8, 14507,~~17, 1240–1248. https://doi.org/10.1038/s41561-024-01582-3, 2024.

Wallis, B. J., Hogg, A. E., ~~ncomms14507, 2017~~Zhu, Y., and Hooper, A.: Change in grounding line location on the Antarctic Peninsula measured

using a tidal motion offset correlation method, The Cryosphere, 18, 4723–4742, https://doi.org/10.5194/tc-18-4723-2024, 2024.

Wegmüller, U., Werner, C., Strozzi, T., Wiesmann, A., Frey, O., and Santoro, M.: Sentinel-1 support in the gamma software, Procedia Comput. Sci., 100, 1305–1312, https://doi.org/10.1016/j.procs.2016.09.246, 2016.

~~Werner, C. L., Wegmüller, U., Strozzi, T., and Wiesmann, A.: Gamma SAR and interferometric processing software, in Proceedings of the ERS645 ENVISAT Symposium, Gothenburg, Sweden, 16–20 October 2000, 1620, 1620, 2000.~~

~~Yoon, S. T., Lee, W. S., Nam, S., Lee, C. K., Yun, S., Heywood, K., et al.: Ice-front retreat reconfigures meltwater-driven gyres modulating ocean heat delivery to an Antarctic ice shelf, Nat. Commun., 13, 306, https://doi.org/10.1038/s41467-022-27968-8, 2022.~~

Zhang, B., Liu, J., Wang, Z., Liu, T., and Yang, Q.: Antarctic ice-shelf thickness changes from CryoSat-2 SARIn mode measurements: Assessment and comparison with IceBridge and ICESat, J. Earth Syst. Sci., 129, 127, https://doi.org/10.1007/s12040-020-01392-2, 2020.

Zhou S., Dutrieux P., Giulivi C. F., Silvano A., Auckland C., Abrahamsen P., et al.: Southern Ocean moored time series (south of 60°S) (OCEAN ICE D1.1). SEANOE. https://doi.org/10.17882/99922, 2024.

Zhou S., Dutrieux P., Giulivi C. F., Jenkins A., Silvano A., Auckland C., et al.: The OCEAN ICE mooring compilation: a standardised, pan-Antarctic database of ocean hydrography and current time series. https://doi.org/10.5194/essd-2025-54, 2025.

Zhu, Y., Hogg, A. E., Hooper, A., and Wallis, B. J.: Short and Long-term Grounding Zone Dynamics of Amery Ice Shelf, East Antarctica, EGUsphere [preprint], https://doi.org/10.5194/egusphere-2025-849, 2025.

Zinck, A.-S. P., Wouters, B., Lambert, E., and Lhermitte, S.: Unveiling spatial variability within the Dotson Melt Channel through high-resolution basal melt rates from the Reference Elevation Model of Antarctica, The Cryosphere, 17, 3785–3801, https://doi.org/10.5194/tc-17-3785-2023, 2023a.

Zinck, A.-S. P.: BURGEE, [Software], GitHub, https://github.com/aszinck/BURGEE, 2023b.